Cardiolipin deficiency disrupts CoQ-complex III interface in steatohepatitis

Marisa J Brothwell, Guoshen Cao, J. Alan Maschek, Annelise M Poss, Alek D Peterlin, Liping Wang, Talia B Baker, Justin L Shahtout, Piyarat Siripoksup, Quentinn J Pearce, et al.

Cardiolipin deficiency disrupts CoQ-complex III interface in steatohepatitis

Marisa J. Brothwell,[1,2] Guoshen Cao,[1,3] J. Alan Maschek,[1,2,4] Annelise M. Poss,[1,2] Alek D. Peterlin,[1,2] Liping Wang,[1,2] Talia B. Baker,[5,6] Justin L. Shahtout,[1,7] Piyarat Siripoksup,[1,7] Quentinn J. Pearce,[4] Jordan M. Johnson,[1,2] Fabian M. Finger,[8,9] Alexandre Prola,[10] Sarah A. Pellizzari,[3,11] Gillian L. Hale,[5,11] Allison M. Manuel,[4] Shinya Watanabe,[1,2] Edwin R. Miranda,[1,2,12] Kajsa E. Affolter,[5,10] Trevor S. Tippetts,[1,2] Linda S. Nikolova,[13] Ran Hee Choi,[1,2,12] Stephen T. Decker,[1,2,12] Mallikarjun Patil,[1,2,12] J. Leon Catrow,[4] William L. Holland,[1,2,3,12] Sara M. Nowinski,[14] Daniel S. Lark,[15,16] Kelsey H. Fisher-Wellman,[17] Patrice N. Mimche,[18] Kimberley J. Evason,[5,11] James E. Cox,[1,3,4] Scott A. Summers,[1,2,3,5,12] Zach Gerhart-Hines,[8,9] Katsuhiko Funai[1,2,3,5,7,12]*

[1]Diabetes & Metabolism Research Center; University of Utah; Salt Lake City, UT; USA.

[2]Department of Nutrition and Integrative Physiology; University of Utah; Salt Lake City, UT; USA.

[3]Department of Biochemistry; University of Utah; Salt Lake City, UT; USA.

[4]Metabolomics Core Research Facility; University of Utah; Salt Lake City, UT; USA.

[5]Huntsman Cancer Institute; University of Utah, Salt Lake City, UT; USA.

[6]Division of Transplantation and Advanced Hepatobiliary Surgery, Department of Surgery; University of Utah; Salt Lake City, UT; USA.

[7]Department of Physical Therapy and Athletic Training; University of Utah; Salt Lake City, UT; USA.

[8]Novo Nordisk Foundation Center for Basic Metabolic Research; University of Copenhagen; Copenhagen; DK.

[9]Center for Adipocyte Signaling (ADIPOSIGN); University of Southern Denmark; Odense; DK.

[10]Laboratory of Fundamental and Applied Bioenergetics; University of Grenoble Alpes, Inserm U1055; Grenoble; FR.

[11]Department of Pathology; University of Utah; Salt Lake City, UT; USA.

[12]Molecular Medicine Program; University of Utah; Salt Lake City, UT; USA.

[13]Electron Microscopy Core Facility; University of Utah; Salt Lake City, UT; USA.

[14]Department of Metabolism and Nutritional Programming; Van Andel Institute; Grand Rapids, MI; USA.

[15]College of Health and Human Sciences; Colorado State University; Fort Collins, CO; USA.

[16]Columbine Health Systems Center for Healthy Aging; Colorado State University; Fort Collins, CO; USA

[17]Department of Cancer Biology, Wake Forest University School of Medicine; Atrium Health Wake Forest Baptist Comprehensive Cancer Center; Winston-Salem, NC; USA.

[18]Departments of Dermatology and Medicine; Division of Gastroenterology and Hepatology, Indiana University School of Medicine; Indianapolis, IN; USA.

*Lead Contact

Correspondence:

Katsuhiko Funai, Ph.D.

kfunai@health.utah.edu

Abstract

Metabolic dysfunction-associated steatotic liver disease (MASLD) is a progressive disorder marked by lipid accumulation, leading to steatohepatitis (MASH). A key feature of the transition to MASH involves oxidative stress resulting from defects in mitochondrial oxidative phosphorylation (OXPHOS). Here, we show that pathological alterations in the lipid composition of the inner mitochondrial membrane (IMM) directly instigate electron transfer inefficiency to promote oxidative stress. Specifically, mitochondrial cardiolipin (CL) was downregulated with MASLD/MASH in mice and in humans. Hepatocyte-specific CL synthase knockout (CLS-LKO) led to spontaneous and robust MASH with extensive steatotic and fibrotic phenotype. Loss of CL paradoxically increased mitochondrial respiratory capacity but also reduced the formation of $I+III_2+IV_1$ respiratory supercomplex and interfered with the ability of coenzyme Q (CoQ) to transfer electrons to complex III. In turn, the bottleneck at complex III promoted electron leak primarily at site III_{Q0} as well as other upstream sites in the electron transport chain. Thus, reduction in mitochondrial CL promotes oxidative stress and contributes to pathogenesis of MASH.

Main

Metabolic dysfunction-associated steatotic liver disease (MASLD) is a growing global health concern with an increasing prevalence that parallels the rise in obesity.[1] In the United States, annual medical costs related to MASLD exceed $103 billion.[2] A large portion of patients with MASLD only exhibit steatosis, a silent and relatively benign early stage characterized by lipid accumulation in hepatocytes without hepatocellular inflammation.[3] Steatosis can then progress to metabolic dysfunction-associated steatohepatitis (MASH), determined by hepatocyte injury and tissue fibrosis.[4] MASH is the last stage of MASLD that may be reversible, making intervention at this stage particularly important.[3,5] Although extensive clinical and basic research have been conducted in this field, the underlying mechanisms by which fatty liver transitions to MASH remain poorly understood.[6-8]

A defect in mitochondrial function is considered one of the hallmarks of MASLD progression in both mice and humans.[9-12] MASLD is initially associated with an increase in mitochondrial respiratory capacity, followed by a subsequent impairment in oxidative phosphorylation (OXPHOS), and increased production of mitochondrial reactive oxygen species (ROS).[11,13] Mitochondrial ROS is thought to be caused by an inefficient electron transport chain (ETC) that increases the propensity for electron leak. However, the mechanisms by which mitochondrial electron leak promotes MASLD are unknown.

Cardiolipin (CL) is a phospholipid with four acyl chains conjugated to two phosphatidylglycerol moieties linked by another glycerol molecule.[14] CL resides almost exclusively in the inner mitochondrial membrane (IMM), constituting approximately 15–20% of the mitochondrial phospholipids.[15] CL is synthesized by the condensation of phosphatidylglycerol (PG) and cytidine diphosphate-diacylglycerol (CDP-DAG) at the IMM via the enzyme cardiolipin synthase (CLS).[16,17] Structural studies indicate that CL is essential for the activities of OXPHOS

enzymes.[18-22] In non-hepatocytes, decreased CL leads to compromised oxidative capacity,[23,24] impaired membrane potential,[25] and altered cristae morphology.[26] In particular, low CL is associated with increased H_2O_2 production.[27,28]

In this manuscript, we set out to examine the changes in liver mitochondrial lipidome induced by MASH. In both mice and in humans, mitochondrial CL was downregulated in livers with MASLD/MASH compared to healthy controls. We then performed a targeted deletion of CLS in hepatocytes and studied its effects on liver, mitochondrial bioenergetics, and potential mechanisms that drive these changes.

Results

Mitochondrial cardiolipin levels are decreased in mouse models of MASLD/MASH

Previous research from our lab in non-hepatocytes indicated that mitochondrial phospholipid composition affects OXPHOS electron transfer efficiency to alter electron leak.[15,29,30] MASLD has been shown to alter the total cellular lipidome in liver.[31] However, MASLD may also influence mitochondrial content in the hepatocytes, making it difficult to discern whether these are changes in the lipid composition of mitochondrial membranes and/or changes in cellular mitochondrial density. Thus, we performed liquid chromatography-tandem mass spectrometry (LC-MS/MS) lipidomics specifically on mitochondria isolated from human liver samples with or without MASH. Samples from patients undergoing liver transplant or resection due to end-stage MASH (Fig. 1a, and Extended Data Table 1) were compared to samples from patients without MASH, undergoing resection for benign liver tumors or metastases (Fig. 1b). Strikingly, mitochondrial CL levels were reduced, primarily due to a decrease in tetralinoleoyl CL (Fig. 1c), commonly thought as the mature and functional form of CL. Additionally, levels of mitochondrial PG, an essential precursor to CL production, were also reduced, suggesting a disruption in CL biosynthesis (Fig. 1d-e).

We next performed lipidomic analyses on four distinct mouse models of MASLD/MASH (Fig. 1f-q). These included: 1) mice given a Western high-fat diet (HFD, Envigo TD.88137) or standard chow diet for 16 weeks (Fig. 1f), 2) ob/ob mice or their wildtype littermates at 20 weeks of age (Fig. 1g), 3) mice given the Gubra Amylin NASH diet for 30 weeks (GAN, Research Diets D09100310) or standard chow (Fig. 1h), 4) mice injected with carbon tetrachloride (CCl_4) or vehicle (corn oil) for 6 weeks (Fig. 1i). Importantly, none of these interventions appear to alter the protein abundances of OXPHOS subunits or citrate synthase (Fig. 1j-m), suggesting that these interventions did not alter mitochondrial density in hepatocytes. Nevertheless, we performed all mitochondrial lipidomic analyses by quantifying lipids per mg of mitochondrial proteins. Each intervention appeared to alter different subsets of mitochondrial lipid classes (Fig. 1n-q, and Extended Data Fig. 1 and 2), as seen with our previous studies in skeletal muscle and brown adipose tissues.[29,30] We take these observations to mean that most physiological interventions induce multiple systemic and local responses that are not mechanistically directly related to the phenotype of interest (e.g., cold exposure or exercise can increase food intake, obesity could affect locomotion and insulation, etc.). Although several phospholipid classes were altered among the four models, strikingly, mitochondrial CL was reduced in all four MASLD/MASH models (Fig. 1n-r). Furthermore, PG was significantly increased in all MASLD/MASH models (Fig. 1n-r). These changes coincided with decreased transcript levels for CLS (Fig. 1s-v). These observations further suggest that an insult in CL synthesis may be a key factor to disrupting mitochondrial function in MASLD/MASH.

Hepatocyte-specific deletion of cardiolipin synthase promotes MASH

CL is thought to be exclusively synthesized in the IMM where CLS is localized. To study the role of CL in hepatocytes, we generated mice with hepatocyte-specific knockout of CLS (CLS-LKO for *CLS l*iver *k*nock*o*ut, driven by albumin-Cre) (Fig. 2a,b), which successfully decreased

mitochondrial CL levels (Fig. 2c, and Extended Data Fig. 3). Consistent with our previous studies in non-hepatocytes, CLS deletion does not completely reduce CL levels to zero, suggesting that CL generated in other tissues may be imported. Our results showed that decreased levels of CL did not significantly impact body weight or composition (Fig. 2d,e) but resulted in significantly less liver mass (Fig. 2f).

We sought to further characterize livers from control and CLS-LKO mice. Histological analyses revealed that CLS deletion was sufficient to promote steatosis (Fig. 2g) and fibrosis (Fig. 2h) in standard chow-fed and high-fat fed conditions (Extended Data Fig. 4a,b). To more comprehensively describe the effects of loss of hepatic CLS on gene expression, we performed RNA sequencing on these livers. CLS deletion increased the expression of 713 genes and decreased 1026 genes (Extended Data Fig. 4c). Pathway analyses revealed that many of the signature changes that occur with MASLD/MASH also occurred with CLS deletion (Fig. 2i, and Extended Data Fig. 4d). This MASLD/MASH phenotype in our CLS knockout model was further confirmed with an elevation of the liver enzymes AST and ALT (Fig. 2j,k) as well as increased mRNA levels of inflammatory markers (Fig. 2l). We then proceeded to confirm these data by further phenotyping liver tissues from control and CLS-LKO mice.

In steatohepatitis, immune cell populations in the liver become altered to activate pathological immune response.[32] Flow cytometry on livers from control and CLS-LKO mice indicated that the loss of CL promotes a robust classic immune response found in MASH (Fig. 2m). cDC2 cells are a broad subset of dendritic cells with specific surface markers (e.g., CD11b, CD172a) that allow them to be distinguished from other dendritic cell populations.[33] This broad population of dendritic cells was not different between control and CLS-LKO mice (Fig. 2n). Notably, there was a marked reduction in the Kupffer cell population (Fig. 2o) - traditionally involved in maintaining liver homeostasis whose dysfunction can lead to dysregulated immune response.[34]

This reduction appears to be counterbalanced by a concomitant increase in Ly6C^{hi} population, which are known to typically go on to become inflammatory monocytes (Fig. 2m,p). The replacement of Kupffer cells with other inflammatory cell populations suggests a shift towards a more pro-inflammatory environment, which may exacerbate liver injury and promote fibrosis. Nonetheless, the MHC-II cell population and neutrophils were not increased (Fig. 2q,r) with neutrophils actually decreased (Fig. 2r). The cDC1 cell population was not different, which is traditionally elevated in response to cytotoxic T cells and might not be directly related to liver fibrosis.[35] Together, these findings suggest that even on a chow diet, CLS-deficient livers exhibit inflammatory cell infiltration, a hallmark often associated with early signs of MASH.

CLS deletion promotes fatty liver but increases mitochondrial respiratory capacity

Hepatocyte lipid accumulation may suggest defects in substrate handling, which is often manifested in systemic substrate handling. Indeed, CLS deletion modestly reduced glucose or pyruvate handling, even in chow-fed conditions (Fig. 3a-d). Lipid accumulation in hepatocytes can occur due to an increase in lipogenesis, a decrease in VLDL secretion, or a decrease in β-oxidation. However, mRNA levels for lipogenesis genes trended lower (not higher), and mostly unchanged for VLDL secretion or β-oxidation (Fig. 3e, and Extended Data Fig. 5a). Circulating triglycerides were not lower in CLS-LKO mice compared to control mice (Extended Data Figure 5b).

MASLD is known to be associated with reduced mitochondrial oxidative capacity, and such an effect may also occur with CL deficiency to induce lipid accumulation. Indeed, mRNA levels of several genes in the ETC were downregulated with CLS deletion, particularly those associated with structural components of the ETC complexes and the electron carrier CoQ (Fig. 3f). Given that CL is located in the IMM where it binds to enzymes involved in OXPHOS,[36-39] we reasoned that the loss of CL could reduce mitochondrial oxidative capacity to promote steatosis.

Consistent with subcellular localization of CL, CLS deletion resulted in mitochondria with disorganized membrane structures and poorly developed cristae (Fig. 3g). However, mitochondrial density quantified with western blots for respiratory complex subunits and citrate synthase (Fig. 3h), as well as mtDNA/nucDNA (Fig. 3i), showed no differences in livers from control and CLS-LKO mice. We thus speculated that CL lowers respiratory capacity not by reducing the total number of mitochondria or OXPHOS respirasomes, but by reducing the activity of respiratory enzymes. To our surprise, CLS deletion increased, rather than decreased, mitochondrial respiration (JO_2), as measured by high-resolution Oroboros respirometry (Fig. 3j), using both with Krebs cycle substrates (Fig. 3k) as well as fatty acyl substrates (Fig. 3l), to a similar degree. Importantly, these changes occurred in the absence of differences in OXPHOS subunit abundance per unit of mitochondria (Fig. 3m), ruling out the possibility that changes in the abundance of respiratory enzymes to contribute to change in respiration. A caveat to these findings is that CLS deletion promotes reduction in respiratory capacity after HFD-feeding (Extended Data Fig. 5c,d). However, CLS-LKO mice are steatotic in standard chow-fed condition, indicating that reduced mitochondrial fatty acid oxidation cannot be the cause of steatosis at baseline. The transient increase in respiration followed by its subsequent decrease is reminiscent of what is thought to occur with liver's mitochondrial respiration over the course of MASLD progression.[40]

High-resolution respirometry experiments were performed in isolated mitochondria from hepatocytes by providing exogenous supraphysiological concentrations of substrates. While these assays provide robust measurements of respiratory capacity (the potential of mitochondria), they do not necessarily reflect their endogenous activity. To address this point, we performed stable isotope tracing experiments using uniformly labeled ^{13}C-palmitate (Fig. 4a)[41] in murine hepa1-6 cells without (scrambled shRNA or shSC) or with CLS knockdown (shRNA targeting CLS or shCLS). Surprisingly, but consistent with the JO_2 data, CLS deletion

increased, not decreased, the incorporation of palmitate into TCA intermediates (Fig. 4b-d). We also performed a similar tracing experiment using uniformally labeled ^{13}C-glucose (Fig. 4e-j, and Extended Data Fig. 5e-i) and observed increased labeling towards pyruvate (Fig. 4e,f), reduced labeling towards lactate and alanine (Fig. 4g, and Extended Data Fig. 5h), and normal labeling towards TCA intermediates except for reduced labeling towards succinate (Fig. 4h-j, and Extended Data Fig. 5i-m). Overall, despite the altered substrate incorporation, a decrease in TCA flux does not appear to account for the steatotic phenotype observed with CLS deletion.

Low hepatic CL paradoxically increases mitochondrial respiratory capacity and promotes electron leak

Oxidative stress is thought to play a critical role in the transition from MASLD to MASH, wherein sustained metabolic insult leads to hepatocellular injury and collagen deposition resulting in fibrosis.[7] CLS deletion promotes liver fibrosis in standard chow-fed condition (Fig. 5a and Fig. 2h) and in HFD-fed condition (Extended Data Fig. 4b) that coincided with increased mRNA levels for fibrosis (Fig. 5b and 2i). Tissue fibrosis is often triggered by apoptosis, and CLS deletion appeared to activate the caspase pathway (Fig. 5c,d). How does deletion of CLS, a mitochondrial enzyme that produces lipids for IMM, activate apoptosis? Cytochrome c is an electron carrier that resides in IMM, which shuttles electrons between complexes III and IV.[42] Under normal physiological conditions, cytochrome c is anchored to the IMM by its binding to cardiolipin.[39] During the initiation of intrinsic apoptosis, CL can undergo oxidation and redistribution from the IMM to the outer membrane space (OMM). CL oxidation weakens its binding affinity for cytochrome c, releasing it from the IMM and into the OMM where it signals apoptosis.[13] However, neither mitochondrial nor cytosolic cytochrome c abundance appeared to be influenced by CLS deletion (Fig. 5e,f, and Extended Data Fig. 6a,b).

Mitochondrial ROS has been implicated in apoptosis and fibrosis with MASLD.[43-45] Using high-resolution fluorometry in combination with high-resolution respirometry, we quantified electron leak from liver mitochondria with the assumption that almost all electrons that leak react with molecular O_2 to produce O_2^-. Using recombinant superoxide dismutase, we ensure that all O_2^- produced is converted into H_2O_2, which was quantified with the AmplexRed fluorophore.[46] There were striking increases in mitochondrial electron leak in CLS-LKO mice compared to control mice on both standard chow (Fig. 5g) and high-fat diet (Extended Data Fig. 6c). It is noteworthy that endogenous antioxidant pathways were insufficient to completely suppress oxidative stress induced by CLS deletion (H_2O_2 emission shown in the 1st and 2nd bars in Fig. 5g, and Extended Data Fig. 6c). We also confirmed that JH_2O_2/JO_2 was elevated with CLS knockdown in mitochondria from murine hepa1-6 cell line (Extended Data Fig. 6d) suggesting that low CL induces oxidative stress in a cell-autonomous manner.

While unknown, CLS may possess an enzymatic activity independent of CL synthesis that may contribute to electron leak. To more conclusively show that the loss of mitochondrial CL contributes to oxidative stress, we supplied exogenous CL to isolated mitochondria by fusing them with small unilamellar vesicles (SUVs) (Fig. 5h).[47] Isolated mitochondria from control and CLS-LKO mice were fused with SUVs containing either CL or phosphatidylcholine (PC) (Fig. 5i, and Extended Data Fig. 6e). Remarkably, reintroducing CL to mitochondria from CLS-LKO mice reduced H_2O_2 production back to baseline, whereas PC had no effect. Thus, loss of CL drives the increased mitochondrial leak observed with CLS deletion.

Loss of CL attenuates coenzyme Q interface with complex III

How does the loss of CL promote electron leak? We first addressed whether CL influences the formations of respiratory supercomplexes. Respiratory supercomplexes exist in several combinations of multimers of Complex I, III, IV, and V and are thought to form either transiently

or stably to improve electron transfer efficiency.[48,49] CL may play an essential role in the stability of ETC supercomplexes.[50,51] Using blue native polyacrylamide gel electrophoresis , we investigated supercomplex assembly in isolated hepatic mitochondria from control and CLS-LKO mice (Fig. 6). When probing indiscriminately for all supercomplexes, there were many bands whose intensity were influenced by CLS deletion (Fig. 6a). In particular, $I+III_2+IV_1$ supercomplex appeared to be substantially and consistently reduced in samples from CLS-LKO mice compared to control. To gain a more granular and definitive picture on the influence of CLS deletion on individual supercomplexes, we quantified supercomplexes using subunit-specific western blotting (Fig. 6b-m). Strikingly, CLS deletion substantially reduced the abundance of $I+III_2+IV_1$ supercomplex when probing for UQCRSF1/complex III (Fig. 6h,i), while increasing the abundances for CIII singlet and CIV singlet (Fig. 6j,k), as well as trends for increase in CI singlet (Fig. 6b-e). These findings suggest that loss of CL reduces $I+III_2+IV_1$ supercomplex assembly to attenuate electron flux through these complexes, promoting electron leak.

To better understand how low CL promotes inefficient electron transfer, we quantified electron leak at four specific sites of the ETC: 1) quinone-binding site in complex I (I_Q), 2) flavin-containing site in complex I (I_F), 3) succinate-dehydrogenase-associated site in complex II (II_F), and 4) the ubiquinol oxidation site in complex (III_{Qo}) Fig. 7a). Electron leak at each of these sites can be quantified separately using substrates and inhibitors that restrict electron flow specific to these sites (Fig. 7b-e). Among complex I, III, and IV (the components of $I+III_2+IV_1$ supercomplex), CLS deletion robustly increased electron leak at site III_{Qo} (Fig. 7e). In addition, electron leak either increased or trended to increase at all other upstream sites (Fig. 7b-d). These findings raise a possibility that inefficient electron transfer at complex III bottlenecks the ETC electron flow to increase electron leak at these sites.

We further examined the possibility that complex III is the primary site of defect induced by CLS deletion, we studied the redox state of CoQ, a career that feeds electrons into complex III. It is noteworthy that CoQ, like CL, is a lipid molecule (Fig. 7f), and we thought it was conceivable that CL somehow interacts with CoQ to influence its electron transfer efficiency. Using redox mass spectrometry, we measured CoQ levels in whole liver tissues from control and CLS-LKO mice and found no difference in whole liver tissue CoQ levels (Extended Data Fig. 7a-i). However, since CoQ may also be found outside of mitochondria, we performed CoQ redox mass spectrometry in isolated mitochondria fractions of livers from control or CLS-LKO mice. Indeed, oxidized CoQ levels were increased (Fig. 7g, and Extended Data Fig. 7j,l,n) in CLS-LKO mice compared to their controls. In contrast, reduced forms of CoQ were not lower in CLS-LKO mice compared to control mice (Fig. 7h, and Extended Data Fig. 7k,m,o). Thus, CLS deletion does not appear to have a defect in converting oxidized CoQ into reduced CoQ (i.e., charging CoQ with electrons by complex I and II). Rather, these data support the notion that the defect is at complex III, as the normal level of reduced CoQ yielded greater oxidized CoQ.

To extrapolate these findings into humans, we went back to liver samples from patients undergoing liver transplant or resection due to end-stage MASH (Fig. 1a) to quantify the abundance of mitochondrial CoQ. MASH was associated with a striking ~40% reduction in the abundance of mitochondrial CoQ (Fig. 7i) (tissue samples were not large enough to perform CoQ redox mass spectrometry on mitochondria). A Pearson correlation analysis showed a highly robust correlation between the abundances of mitochondrial CL and CoQ (Figure 7j, R^2 = 0.64), indicating that the variability in the abundance of CL explains 64% of the variability of the abundance of CoQ. Based on our findings that CL is reduced with MASLD/MASH and that loss of CL influences CoQ electron transfer efficiency, we interpret these findings to mean that loss of CL destabilizes CoQ to increase its turnover.

Discussion

In hepatocytes, disruptions of mitochondrial bioenergetics lead to and exacerbate metabolic-associated steatohepatitis.[52] CL, a key phospholipid in the inner mitochondrial membrane, plays a critical role in mitochondrial energy metabolism.[23] In this manuscript, we examined the role of CL in the pathogenesis of MASLD. In mice and in humans, MASLD/MASH coincided with a reduction in mitochondrial CL levels. Hepatocyte-specific deletion of CLS was sufficient to spontaneously induce MASH pathology, including steatosis and fibrosis, along with shift in immune cell populations towards a more pro-inflammatory profile, all of which occurred in mice given a standard chow diet. Paradoxically, high-resolution respirometry and stable isotope experiments showed that CLS deletion promotes, instead of attenuates, mitochondrial oxidative capacity in a fashion reminiscent of temporal changes that occur with mitochondrial bioenergetics in human MASH.[40] Our principal finding on the role of hepatocyte CL in bioenergetics is that its loss robustly increases electron leak, particularly at complex III. This was likely due to: 1) direct interaction of CL with complex III, 2) lower abundance of $I+III_2+IV_1$ respiratory supercomplex, and 3) inability of complex III to efficiently accept electrons from CoQ. In humans, mitochondrial CL and CoQ were co-downregulated in MASH patients compared to healthy controls, with a strong correlation ($R^2 = 0.64$) between CL and CoQ. Together, these results implicate CL as a key regulator of MASH progression, particularly through its effect on the CoQ-complex III interface to promote oxidative stress.

How might CL regulate CoQ? CoQ is the main electron transporter between complex I/II and III. CLS deletion in hepatocytes appeared to disrupt CoQ's ability to cycle between its oxidized and reduced forms. There are several ways in which low CL might directly or indirectly influence CoQ’s redox state. The primary suspect is CL interacting with complex III, as eight or nine CL molecules are tightly bound to complex III[38] and are thought to be essential to its function.[53] While CL has been found to bind to other respiratory complexes, our data suggest that loss of

CL might disproportionately influence complex III. This is also supported by our findings that the loss of CL reduced the formation of complex III-dependent supercomplex, without influencing other supercomplexes. Reduced capacity for complex III to efficiently accept electrons from CoQ might explain the increased electron leak at site III_{Q0} and increased level of oxidized CoQ. Meanwhile, loss of CL also increased electron leak at complex I and II. CL has also been implicated to bind to these complexes.[20,21,36] Thus, complex III dysfunction is perhaps unlikely to entirely explain electron leaks at sites I_F, I_Q, and II_F, though we think that the majority of its effect is due to the bottleneck created by the reduced ability of complex III to accept electrons.[54] Conversely, complex I and II are unlikely to be the only primary sites of defect as such defects probably will not promote electron leak at site III_{QO}. Moreover, CLS deletion did not have an effect on the abundance of reduced CoQ despite there being greater abundance of oxidized CoQ, suggesting that complex I/II do not have reduced ability to transfer electrons onto CoQ. Another potential mechanism by which CL influences CoQ redox state is by CL directly interacting with CoQ. As they are both lipid molecules in the IMM, low CL may reduce the lateral diffusability of CoQ between respiratory complexes. Low CL might also indirectly influence CoQ by contributing to changes in membrane properties, distribution of ETC in the cristae, and the cristae architecture.[55] Finally, increased electron leak, regardless of their origin, could have a feed-forward effect by which oxidative stress disrupts redox homeostasis in other components of ETC.

MASH is a progressive liver disease characterized by lipid accumulation, inflammation, and fibrosis in the liver.[56] The progression to MASH involves a complex interplay of metabolic stress, mitochondrial defects, and immune responses that collectively promote hepatocellular injury.[57] Our findings suggest that a low mitochondrial CL level directly induces key pathological features of MASH, including steatosis, fibrosis, and immune cell infiltration, even in the absence of dietary or environmental stressors, such as high-fat diet. When mice were fed a standard chow

diet, CLS-LKO mice were more prone to lipid droplet accumulation than control mice. This phenotype was exacerbated when the mice were challenged with a high-fat diet. We primarily interrogated the mitochondrial bioenergetics of standard chow-fed control or CLS-LKO mice. A lower respiration rate would partially explain the lipid droplet accumulation, but to our surprise, CLS deletion increased JO_2 regardless of substrates. Similarly, experiments using uniformly labeled ^{13}C-palmitate or ^{13}C-glucose showed that CLS deletion promoted an overall increase in the flux toward TCA intermediates, particularly for palmitate. CLS deletion did not appear to increase de novo lipogenesis or reduce VLDL secretion. Thus, it is unclear what mechanisms contribute to steatosis induced by CLS deletion.

Liver fibrosis is characterized by the accumulation of excess extracellular matrix components, including type I collagen, which disrupts liver microcirculation and leads to injury.[55] Livers from CLS-LKO mice exhibited more fibrosis compared to control mice, even on a standard chow diet, which was worsened when fed a high-fat diet. Indeed, transcriptomic analyses revealed that CLS deletion activates pathways for fibrosis and degeneration, with many of the collagen isoforms upregulated. In the MASH liver, collagen deposition is accompanied by inflammatory cell infiltrate promoting an overall inflammatory environment. Flow cytometry experiments further confirmed that CLS deletion led to an increase in Ly6C^{hi} cell population, suggesting that dying resident Kupffer cells are being replaced by Ly6C^{hi} monocytes in the livers of CLS-LKO mice.[33]

Early in the MASLD disease progression, mitochondria adapt to the increased energy demands by increasing their respiratory capacity. In the later stages of disease progression to MASH, mitochondrial respiration diminishes.[58] This pattern was reminiscent of our observations in the CLS-LKO mice. Livers from CLS-LKO mice fed a standard chow diet exhibited greater respiratory capacity compared to that of control mice. Conversely, livers from CLS-LKO mice on

a high-fat diet exhibited lower respiratory capacity compared to that of control mice. We interpret these findings to suggest that liver mitochondria in chow-fed CLS-LKO mice are more representative of early stage of MASLD, while high-fat-diet fed CLS-LKO mice resemble later stages of MASLD.

In non-hepatocytes, low CL levels have been linked to electron leak in the context of a deficiency of the tafazzin gene, a CL transacylase, whose mutation promotes Barth syndrome.[15,26,59,60] Paradoxically, we previously showed that CLS deletion in brown adipocytes does not increase electron leak.[30] It is important to note that CLS deletion in our current or previous study does not completely eliminate CL (likely due to an extracellular source). We do not believe that CL is dispensable for efficient electron transfer in adipocytes. Rather, due to unclear mechanisms, different cell types likely exhibit varying tolerances to low CL influencing their bioenergetics, with brown adipocytes appearing more tolerant than hepatocytes. Regardless, electron leak was elevated with CLS deletion in both standard chow and high-fat diet-fed conditions. These observations mirror what has been shown in MASLD progression.[61] The effect of CLS deletion on electron leak was due to reduced CL levels, as the reintroduction of cardiolipin via SUVs completely rescued the electron leak.

CL is reported to be essential for the formation and stability of supercomplexes.[14,50,51,62] CL has a distinctive conical shape with four fatty acyl chains, which allows it to create a highly curved membrane environment in the IMM, promoting close packing of protein complexes that likely facilitates supercomplex formation.[50] CL also directly interacts with various subunits of the ETC complexes through electrostatic interactions, which help stabilize the supercomplexes by anchoring them together in a specific spatial orientation to optimize electron flow.[48] Liver-specific deletion of CLS only resulted in a lower abundance of the $I+III_2+IV_1$ supercomplex. We

interpret these findings to mean that I+III_2+IV_1 supercomplex is particularly sensitive to the reduced CL level in hepatocytes.

In our study, we observed a striking correlation between CL levels and CoQ in human liver samples from healthy/MASH patients (R_2 of 0.64). In contrast, low mitochondrial CL induced by CLS deletion coincided with a greater mitochondrial CoQ content in CLS-LKO mice compared to controls. These data likely suggest that acute and robust reduction in CLS or CL level might trigger a compensatory CoQ production in mice. Conversely, because the samples from healthy/MASH patients were from those who had cirrhosis, MASH samples likely came from subjects that had suffered from years of MASLD pathology. In those samples, where reduction in CL was quantitatively modest compared to what was induced with CLS knockout, CoQ might have gradually decreased coincidental to the decrease in CL. Regardless of these differences in mice and humans, it is clear that there is a relationship between CL and CoQ that is worth further exploration.

In conclusion, our findings identify a critical role for CL in regulating ETC efficiency to promote oxidative stress. In both mice and humans, MASLD is associated with a decrease in hepatic mitochondrial CL, suggesting that low CL may be the cause of the obligatory increase in oxidative stress known to occur with MASLD progression. We further link CL deficiency to increased electron leak at the CoQ-complex III interface, and as the primary defect that promotes oxidative stress. We believe that these bioenergetic changes underlie the pathogenesis of MASLD, as CL deletion was sufficient to cause steatosis, fibrosis, and inflammation, phenocopying many changes that occur with MASLD/MASH progression. Further research will be needed to fully uncover how CL regulates CoQ, and to test whether rescuing the CL/CoQ axis might be effective in treating patients with MASLD/MASH.

Methods

Experimental model and subject details

Human participants

De-identified liver samples were acquired from the University of Utah Biorepository and Molecular Pathology Shared Resource from patients undergoing liver transplantation or resection due to end-stage liver disease and/or liver tumor(s). All patients were classified to their respective diagnosis by a pathologist at the time of initial collection. The diagnosis for individual tissue samples was confirmed by a pathologist based on histology review of formalin-fixed, paraffin-embedded sections takes from the same location as the tissue analyzed by targeted lipid mass spectrometry.

Mice

All mice (male and female) used in this study were bred onto C57BL/6J background. CLS-LKO mice were generated by crossing the CLS conditional knockout ($CLScKO^{+/+}$) generously donated by Dr. Zachary Gerhart-Hines (University of Copenhagen)[24] with mice heterozygous for Albumin promotor Cre ($Alb\text{-}Cre^{+/-}$) to produce liver-specific deletion of the CLS gene ($CLScKO^{+/+}$, $Alb\text{-}Cre^{+/-}$) or control ($CLScKO^{+/+}$, no Cre) mice. $CLScKO^{+/+}$ mice harbor loxP sites that flank exon 4 of the CLS gene. For high-fat diet studies, 8 wk CLS-LKO and their respective controls began high-fat diet (HFD, 42% fat, Envigo TD.88137) feeding for 8 wks. Mice were fasted 4 hours and given an intraperitoneal injection of 80 mg/kg ketamine and 10 mg/kg xylazine prior to terminal experiments and tissue collection. All animal experiments were performed with the approval of the Institutional Animal Care and Use Committees at the University of Utah.

Cell lines

Hepa 1-6 murine hepatoma cells were grown in high-glucose DMEM (4.5 g/L glucose, with L-glutamine; Gibco 11965-092) supplemented with 10% FBS (heat-inactivated, certified, US origin; Gibco 10082-147), and 0.1% penicillin-streptomycin (10,000 U/mL; Gibco 15140122). For lentivirus-mediated knockdown of CLS, CLS expression was decreased using the pLKO.1 lentiviral-RNAi system. Plasmids encoding shRNA for mouse *Crls1* (shCLS: TRCN0000123937) was obtained from MilliporeSigma. Packaging vector psPAX2 (ID 12260), envelope vector pMD2.G (ID 12259), and scrambled shRNA plasmid (SC: ID 1864) were obtained from Addgene. HEK293T cells in 10 cm dishes were transfected using 50 µL 0.1% polyethylenimine, 200 µL, 0.15 M sodium chloride, and 500 µL Opti-MEM (with HEPES, 2.4 g/L sodium bicarbonate, and l-glutamine; Gibco 31985) with 2.66 µg of psPAX2, 0.75 µg of pMD2.G, and 3 µg of either scrambled or *Crls1* shRNA plasmid. Cells were selected with puromycin throughout differentiation to ensure that only cells infected with shRNA vectors were viable.

Method details

Body composition

To assess body composition, mice were analyzed using a Bruker Minispec NMR (Bruker, Germany) 1 week prior to terminal experiments. Body weights were measured and recorded immediately prior to terminal experiments.

RNA quantification

For quantitative polymerase chain reaction (qPCR) experiments, mouse tissues were homogenized in TRIzol reagent (Thermo Fisher Scientific) and RNA was isolated using standard techniques. The iScript cDNA Synthesis Kit was used to reverse transcribe total RNA, and qPCR was performed with SYBR Green reagents (Thermo Fisher Scientific). Pre-validated primer sequences were obtained from mouse primer depot (https://mouseprimerdepot.nci.nih.gov/). All mRNA levels were normalized to RPL32. For RNA

sequencing, liver RNA was isolated with the Direct-zol RNA Miniprep Plus kit (Zymo Cat#: R2070). RNA library construction and sequencing were performed by the High-Throughput Genomics Core at the Huntsman Cancer Institute, University of Utah. RNA libraries were constructed using the NEBNext Ultra II Directional RNA Library Prep with rRNA Depletion Kit (human, mouse rat). Sequencing was performed using the NovaSeq S4 Reagent Kit v1.5 150x150 bp Sequencing with >25 million reads per sample using adapter read 1: AGATCGGAAGAGCACACGTCTGAACTCCAGTCA and adapter read 2: AGATCGGAAGAGCGTCGTGTAGGGAAAGAGTGT. Pathway analyses were performed by the Bioinformatics Core at the Huntsman Cancer Institute, University of Utah using the Reactome Pathway Database. For differentially expressed genes, only transcripts with Padj < 0.05 and baseMean > 100 are included.

DNA isolation and quantitative PCR

Genomic DNA for assessments of mitochondrial DNA (mtDNA) was isolated using a commercially available kit according to the manufacturer's instructions (69504, Qiagen). Genomic DNA was added to a mixture of SYBR Green (Thermo Fisher Scientific) and primers. Sample mixtures were pipetted onto a 3840well plate and analyzed with QuantStudio 12K Flex (Life Technologies). The following primers were used: mtDNA fwd, TTAAGA-CAC-CTT-GCC-TAG-CCACAC; mtDNA rev, CGG-TGG-CTG-GCA-CGA-AAT-T; nucDNA fwd, ATGACG-ATA-TCG-CTG-CGC-TG; nucDNA rev, TCA-CTT-ACC-TGGTGCCTA-GGG-C.

Western blot analysis

For whole liver lysate, frozen liver was homogenized in a glass homogenization tube using a mechanical pestle grinder with homogenization buffer (50 mM Tris pH 7.6, 5 mM EDTA, 150 mM NaCl, 0.1% SDS, 0.1% sodium deoxycholate, 1% triton X-100, and protease inhibitor cocktail). After homogenization, samples were centrifuged for 15 min at 12,000 × g. Protein

concentration of supernatant was then determined using a BCA protein Assay Kit (Thermo Scientific). Equal protein was mixed with Laemmeli sample buffer and boiled for 5 mins at 95°C for all antibodies except for OXPHOS cocktail antibody (at room temp for 5 mins), and loaded onto 4–15% gradient gels (Bio-Rad). Transfer of proteins occurred on a nitrocellulose membrane and then blocked for 1 hr. at room temperature with 5% bovine serum albumin in Tris-buffered saline with 0.1% Tween 20 (TBST). The membranes were then incubated with primary antibody (see Extended Data Table 2), washed in TBST, incubated in appropriate secondary antibodies, and washed in TBST. Membranes were imaged utilizing Western Lightning Plus-ECL (PerkinElmer) and a FluorChem E Imager (Protein Simple). For isolated mitochondria, identical procedures were taken with equal protein of mitochondrial preps.

Single cell preparation of liver tissue for flow cytometry

After mice were euthanized using isoflurane, blood was collected by cardiac puncture, the abdomen was exposed and the liver collected, rinse with PBS and weighed. Liver was subsequently transferred in approximately 3ml of serum-free RPMI-1640 containing Collagenase D (10mg/ml; Sigma) and DNase (1mg/ml; Sigma) and incubated in a rocking platform for 45 min at 37°C. The liver extract was mashed through a 70µm filter, the cell re-suspended in RPMI-1640 containing 10% FBS and centrifuged at 1600 rpm for 5 min. The supernatant was discarded and the pellet re-suspended in approximately 4 ml of 70% Percoll, then transferred in 15 ml conical tube, carefully overlayed with 4 ml of 30% Percoll and centrifuged 1600 rpm for 25 min with the brake turned off. The non-parenchymal cells suspension from the Percoll interface were removed and mixed with 10 mL of RPMI-1640 containing 10% FBS and the cells were centrifuged at 1600 rpm for 5 min. Red blood cells (RBC) were removed from the pelleted single cell suspensions of livers non-parenchymal cells by incubation in an ammonium chloride -based 1x RBC lysis buffer (Thermofisher, eBioscience). The cells were again pelleted and mixed with FACS buffer (2% BSA, 2mM EDTA in PBS), then

stained with Zombie-NIR viability dye (BioLegend) per manufacturer's instructions to discriminate live vs dead cells. To prevent non-specific Fc binding, the cells were incubated with Fc Block (anti-mouse CD16/32, clone 93, Biolegend) for 15 min followed by the indicated antibodies cocktail for 60 min in the dark on ice: CD45 (FITC, clone S18009F, Biolegend), CD11b (BVC421, clone M1/70, Biolegend), F4/80 (APC, clone BM8, Biolegend), TIM4 (PerCP/Cy5.5, clone RMT4-54, Biolegend), Ly6C (PE, clone HK1.4, Biolegend), MHCII (BV605, clone M5/114.15.2, Biolegend), CD11c (BV785, clone N418, Biolegend) and Ly6G (PE/Cy7, clone 1A8, Biolegend). After surface staining, cells were fixed with a paraformaldehyde-based fixation buffer (BioLegend). Flow cytometric acquisition was performed on a BD Fortessa X20 flow cytometer (BD Biosciences) and data analyzed using FlowJo software (Version 10.8.1; Tree Star Inc).

Glucose tolerance test

Intraperitoneal glucose tolerance tests were performed by injection of 1 mg glucose per gram body mass at least 6 days prior to sacrifice. Mice were fasted for 4 hours prior glucose injection. Blood glucose was measured 30 minutes before glucose injection and at 0, 15, 30, 60, 90, and 120 minutes after injection via tail bleed with a handheld glucometer (Bayer Contour 7151H).

Pyruvate tolerance test

Pyruvate tolerance tests were performed by injection of 2 mg pyruvate per gram of body mass in PBS adjusted to pH 7.3-7.5 at least 6 days prior to sacrifice. Blood glucose was measured 30 minutes before pyruvate injection and at 0, 15, 30, 45, 60, 75, 90, 105, and 120 minutes after injection via tail bleed with a handheld glucometer (Bayer Contour 7151H).

Electron microscopy

To examine mitochondrial ultrastructure and microstructures, freshly dissected liver tissues from CLS-LKO and their controls were sectioned into ≈2 mm pieces and processed by the Electron Microscopy Core at University of Utah. To maintain the ultrastructure of the tissue via irreversible cross-link formation, each section was submerged in fixative solution (1% glutaraldehyde, 2.5% paraformaldehyde, 100 mM cacodylate buffer pH 7.4, 6 mM CaCl2, 4.8% sucrose) and stored at 4°C for 48 hours. Samples then underwent 3 × 10-minute washes in 100 mM cacodylate buffer (pH 7.4) prior to secondary fixation (2% osmium tetroxide) for 1 hour at room temperature. Osmium tetroxide as a secondary fixative has the advantage of preserving membrane lipids, which are not preserved using aldehyde, alone. After secondary fixation, samples were subsequently rinsed for 5 minutes in cacodylate buffer and distilled H_2O, followed by prestaining with saturated uranyl acetate for 1 hour at room temperature. After prestaining, each sample was dehydrated with a graded ethanol series (2 × 15 minutes each: 30%, 50%, 70%, 95%; then 3 × 20 minutes each: 100%) and acetone (3 × 15 minutes) and were infiltrated with EPON epoxy resin (5 hours 30%, overnight 70%, 3 × 2-hour 40 minute 100%, 100% fresh for embed). Samples were then polymerized for 48 hours at 60°C. Ultracut was performed using Leica UC 6 ultratome with sections at 70 nm thickness and mounted on 200 mesh copper grids. The grids with the sections were stained for 20 minutes with saturated uranyl acetate and subsequently stained for 10 minutes with lead citrate. Sections were examined using a JEOL 1200EX transmission electron microscope with a Soft Imaging Systems MegaView III CCD camera.

Histochemistry

A fresh liver tissue was taken from each mouse and immediately submerged in 4% paraformaldehyde for 12 hours and then 70% ethanol for 48 hours. Tissues were sectioned at 10-μm thickness, embedded in paraffin, and stained for Masson’s Trichrome to assess fibrosis

or hematoxylin and eosin (H&E) to determine fat droplet accumulation. Samples were imaged on Axio Scan Z.1 (Zeiss).

Native PAGE

Isolated mitochondria (100 µg) suspended in MIM were pelleted at 12,000 x g for 15 min and subsequently solubilized in 20 µL sample buffer (5 µL of 4x Native Page Sample Buffer, 8 µL 10% digitonin, 7 µL ddH_2O per sample) for 20 min on ice and then centrifuged at 20,000 x g for 30 mins at 4°C. 15 µL of the supernatant (75 µg) was collected and placed into a new tube and mixed with 2 µL of G-250 sample buffer additive. Dark blue cathode buffer (50 mLs 20X Native Page running buffer, 50 mLs 20x cathode additive, 900 mLs ddH_2O) was carefully added to the front of gel box (Invitrogen Mini Gel Tank A25977) and anode buffer (50 mLs 20x Native Page running buffer to 950 mL ddH_2O) was carefully added to the back of the gel box making sure to not mix. The samples were then loaded onto a native PAGE 3-12% Bis-Tris Gel (BN1001BOX, Thermo Fisher Scientific), and electrophoresis was performed at 150 V for 1 hour on ice. The dark blue cathode buffer was carefully replaced with light blue cathode buffer (50 mLs 20X Native Page running buffer, 5 mL 20X cathode additive to 945 mLs ddH_2O) and run at 30 V overnight at 4°C. Gels were subsequently transferred to PVDF at 100 V, fixed with 8% acetic acid for 5 min, washed with methanol, and blotted with the following primary antibodies Anti-GRIM19 (mouse monoclonal; ab110240), Anti-SDHA (mouse monoclonal; ab14715), Anti-UQCRFS1 (mouse monoclonal; ab14746), Anti-MTCO1 (mouse monoclonal; ab14705), Anti-ATP5a (mouse monoclonal; ab14748), Anti-NDUFA9 (mouse monoclonal; ab14713) in 5% non-fat milk in TBST. Secondary anti-mouse HRP antibody listed in the key resources table and Western Lightning Plus-ECL (PerkinElmer NEL105001) was used to visualize bands.

Isolation of mitochondrial and cytosolic fractions

Liver tissues were minced in ice-cold mitochondrial isolation medium (MIM) buffer [300 mM sucrose, 10 mM Hepes, 1 mM EGTA, and bovine serum albumin (BSA; 1 mg/ml) (pH 7.4)] and gently homogenized with a Teflon pestle. To remove excess fat in the samples, an initial high-speed spin was performed on all samples: homogenates were centrifuged at 12,000 x g for 10 mins at 4°C, fat emulsion layers were removed and discarded, and resulting pellets were resuspended in MIM + BSA. Samples were then centrifuged at 800 x g for 10 min at 4°C. The supernatants were then transferred to fresh tubes and centrifuged again at 1,300 x g for 10 min at 4°C. To achieve the mitochondrial fraction (pellet), the supernatants were again transferred to new tubes and centrifuged at 12,000 x g for 10 min at 4°C. The resulting crude mitochondrial pellets were washed three times with 0.15 M KCl to remove catalase, and then spun a final time in MIM. The final mitochondrial pellets were resuspended in MIM buffer for experimental use. For cytosolic fraction, the supernatant from 12,000 x g spin was ultracentrifuged at 180,000 x g for 16 hours in a fixed angle rotor (FIBERLite, F50L-24x1.5). The top half of the supernatant was collected as analyzed as the cytosolic fraction for western blotting analyses.

Mitochondrial respiration measurements

Mitochondrial O_2 utilization was measured using Oroboros O2K Oxygraphs. Isolated mitochondria (50 µg for TCA substrate respiration and 100 µg for fatty acid respiration) were added to the oxygraph chambers containing assay buffer Z (MES potassium salt 105 mM, KCl 30 mM, KH_2PO_4 10 mM, $MgCl_2$ 5 mM, BSA 1 mg/ml). Respiration was measured in response to the following substrates: 0.5 mM malate, 5 mM pyruvate, 2.5 mM ADP, 10 mM succinate, 1.5 µM FCCP, 0.02 mM palmitoyl-carnitine, 0.5 mM malate.

Mitochondrial JH_2O_2

Mitochondrial H_2O_2 production was determined in isolated mitochondria from liver tissue using the Horiba Fluoromax-4/The Amplex UltraRed (10 µM)/horseradish peroxidase (3 U/ml)

detection system (excitation/emission, 565:600, HORIBA Jobin Yvon Fluorolog) at 37°C. Mitochondrial protein was placed into a glass cuvette with buffer Z supplemented with 10 mM Amplex UltraRed (Invitrogen), 20 U/mL CuZn SOD). Since liver tissue is capable of producing resorufin from amplex red (AR), without the involvement of horseradish peroxidase (HRP) or H_2O_2, phenylmethylsulfonyl fluoride (PMSF) was included to the experimental medium due to its ability to inhibit HRP-independent conversion of AR to resorufin.[63] PMSF was added to the cuvette immediately prior to measurements and at a concentration that does not interfere with biological measurements (100 µM).[63] A 5-min background rate was obtained before adding 10 mM succinate to the cuvette to induce H_2O_2 production. After 4 min, 100 µM 1,3-bis(2-chloroethyl)-1-nitrosourea (BCNU) was added to the cuvette with 1 µM auranofin to inhibit glutathione reductase and thioredoxin reductase, respectively. After an additional 4 min, the assay was stopped, and the appearance of the fluorescent product was measured.

Site-specific electron leak was measured by systematically stimulating each site while inhibiting the other three.[54] Site I_F was investigated in the presence of 4 mM malate, 2.5 mM ATP, 5 mM aspartate, and 4 µM rotenone; site I_Q was measured as a 4 µM rotenone-sensitive rate in the presence of 5 mM succinate; site III_{QO} was measured as a 2 µM myxothiazol-sensitive rate in the presence of 5 mM succinate, 5 mM malonate, 4 µM rotenone, and 2 µM antimycin A; and site II_F was measured as the 1 mM malonate-sensitive rate in the presence of 0.2 mM succinate and 2 µM myxothiazol. As previously mentioned, electron leak is quantified using Amplex Red in the presence of excess superoxide dismutase, such that both superoxide and hydrogen peroxide production are accounted for by a change in fluorescence intensity (JH_2O_2) using high-resolution fluorometry (Horiba Fluoromax4®).

Lipid mass spectrometry for reduced and oxidized CoQ

Liver tissue was homogenized in ice cold isolation buffer (250 mM sucrose, 5 mM Tris-HCl, 1 mM EGTA, 0.1% fatty acid free BSA, pH 7.4, 4°C) using a tissuelyser. Mitochondria were then isolated via differential centrifugation (800 x g for 10 min, 1300 x g for 10 min, 12,000 x g for 10 min at 4°C), flushing each step under a stream nitrogen to prevent oxidation. Protein content was determined by bicinchoninic acid assay using the Pierce BCA protein assay with bovine serum albumin as a standard. To extract CoQ from mitochondria, incubations of 100 µg mitochondrial protein in 250 µL ice-cold acidified methanol, 250 µL hexane, and 1146 pmol per sample of CoQ standard (Cambridge Isotope Laboratories, CIL DLM-10279) were vortexed. The CoQ-containing hexane layer was separated by centrifugation (10 min, 17,000 x g, 4°C) and then dried down under a stream of nitrogen. Dried samples were then resuspended in methanol containing 2 mM ammonium formate and transferred to 1.5 mL glass mass spectrometry vials. Liquid chromatography-mass spectrometry (LC-MS/MS) was then performed on the reconstituted lipids using an Agilent 6530 UPLC-QTOF mass spectrometer.

U-^{13}C-glucose and U-^{13}C-palmitate labeling in hepa1-6 cell line

Stable isotope tracing experiments were conducted using U-^{13}C-glucose or U-^{13}C-palmitate to assess metabolic fluxes in hepa1-6 cells with or without CLS knockdown. Cells were incubated in either U-^{13}C-glucose or U-^{13}C-palmitate for 4 hours. For palmitate incubations, U-^{13}C-palmitate was conjugated to fatty acid-free bovine serum albumin (BSA) and supplemented with 1 mM carnitine prior to being added to the culture medium. Following the 4-hour incubation period, cells were washed once with 1 mL of ice-cold Dulbecco's Phosphate Buffered Saline (dPBS) and then scraped in 0.7 mL ice-cold dPBS. The cells were pelleted by centrifugation at 500 x g for 5 minutes at 4°C, and the supernatant was carefully removed. Cell pellets were resuspended in 215 µL of ice-cold dPBS and sonicated on ice using a 1/8” probe sonicator at 30% amplitude for 6 seconds. Debris was lightly pelleted by centrifugation at 500 x g for 2 minutes at 4°C. From the resulting supernatant, 25 µL was transferred to a separate tube for

703 protein quantification using the bicinchoninic acid (BCA) assay. Samples incubated with U-^{13}C-
704 glucose were submitted for gas chromatography-mass spectrometry (GC-MS) and liquid
705 chromatography-mass spectrometry (LC-MS) analysis, while those incubated with U-^{13}C-
706 palmitate were submitted for GC-MS analysis only.
707
708 **GC-MS**
709 All GC-MS analysis was performed with an Agilent 5977b GC-MS MSD-HES and an Agilent
710 7693A automatic liquid sampler. Dried samples were suspended in 40 µL of a 40 mg/mL O-
711 methoxylamine hydrochloride (MOX) (MP Bio #155405) in dry pyridine (EMD Millipore
712 #PX2012-7) and incubated for one hour at 37 °C in a sand bath. 25 µL of this solution was
713 added to auto sampler vials. 60 µL of N-methyl-N-trimethylsilyltrifluoracetamide (MSTFA with
714 1% TMCS, Thermo #TS48913) was added automatically via the auto sampler and incubated for
715 30 minutes at 37 °C. After incubation, samples were vortexed and 1 µL of the prepared sample
716 was injected into the gas chromatograph inlet in the split mode with the inlet temperature held at
717 250 °C. A 10:1 split ratio was used for analysis for most metabolites. Any metabolites that
718 saturated the instrument at the 10:1 split was analyzed at a 100:1 split ratio. The gas
719 chromatograph had an initial temperature of 60 °C for one minute followed by a 10 °C/min ramp
720 to 325 °C and a hold time of 10 minutes. A 30-meter Agilent Zorbax DB-5MS with 10 m
721 Duraguard capillary column was employed for chromatographic separation. Helium was used as
722 the carrier gas at a rate of 1 mL/min.
723
724 Data were collected using MassHunter software (Agilent). Metabolites were identified and their
725 peak area was recorded using MassHunter Quant. This data was transferred to an Excel spread
726 sheet (Microsoft, Redmond WA). Metabolite identity was established using a combination of an
727 in-house metabolite library developed using pure purchased standards, the NIST library and the

Fiehn library. There are a few reasons a specific metabolite may not be observable through GC-MS.

LC-MS

A pooled quality control (QC) sample for each sample type was prepared by combining 10 µL of each sample. Samples were randomized prior to analysis. A SCIEX 7600 Zeno-ToF (AB SCIEX LLC, Framingham, MA, USA) coupled to an Agilent 1290 Infinity II HPLC system in positive-ionization modes was used for analysis. Separation was achieved using a Waters BEH zhilic 2.1 x 100 mm column (Waters Corporation, Milford, MA, USA) with Phenomenex Krudkatcher Ultra (Phenomenex, Torrence, CA, USA). Buffers consisted of 99% ACN with 5% ddH2O (buffer B) and 5% 25 mM ammonium carbonate in ddH2O (buffer A). An initial concentration of 99% buffer B was decreased to 85% over 2 min, then further decreased to 75%, and 60% over 3-minute intervals. Next, buffer B was decreased to 40% and held for 1 min. Then Buffer B was decreased to 1% and held for 1 min. Eluents were returned to initial conditions over 0.1 min, and the system was allowed to equilibrate for 5 min between runs. Mass spectrometry analysis was performed by high-resolution multiple reaction monitoring (MRM HR).

Data was collected using SCIEX analyst. Chromatogram integration was performed using SCIEX MultiQuant. This data was transferred to an Excel spread sheet (Microsoft, Redmond WA). Statistical analysis was performed using Microsoft Excel Data Analysis add-in. The metabolite lists were curated to the metabolites of interest for the researcher as applicable. Metabolite identity was established using a combination of an in-house metabolite library developed using pure purchased standards and the human metabolite data base (hmdb.ca). Isotope correction was performed using in-house software.

Mitochondrial phospholipids enrichment

Isolated mitochondria (500 µg) from 2-month-old mice were incubated in fusion buffer [220 mM mannitol, 70 mM sucrose, 2 mM Hepes, 10 mM KH2PO4, 5 mM MgCl2, 1 mM EGTA, 10 mM glutamate, 2 mM malate, 10 mM pyruvate, and 2.5 mM ADP (pH 6.5)] for 20 min at 30°C under constant stirring agitation in the presence of 15 nmol of small unilamellar vesicles (SUVs) (CL from Avanti Polar Lipids, 840012; PC from Avanti Polar Lipids, 850375C). After fusion, mitochondria were layered on a sucrose gradient (0.6 M) and centrifuged 10 min at 10,000g at 4°C to remove SUV. Pellet was then washed in mitochondrial buffer [250 mM sucrose, 3 mM EGTA, and 10 mM tris-HCl, (pH 7.4)].

Serum AST and ALT

Mice were sacrificed by CO_2 inhalation and blood samples collected via cardiac puncture into heparin-coated tubes and centrifuged for collection of plasma within 1 hour of blood collection and frozen at -80^{o}C until analysis. Plasma samples from mice were processed in a single batch for determination of serum alanine aminotransferase (ALT) and aspartate aminotransferase (AST) levels using a DC Element chemistry analyser (HESKA).

Quantification and statistical analyses

The level of significance was set at $p < 0.05$. Student's T tests were used to determine the significance between experimental groups and two-way ANOVA analysis followed by a within-row pairwise comparison post hoc test where appropriate. For Student's T tests, Gaussian distribution was assumed as well as assuming both populations had the same standard deviation. The sample size (n) for each experiment is shown in the figure legends and corresponds to the sample derived from the individual mice or for cell culture experiments on an individual batch of cells. Unless otherwise stated, statistical analyses were performed using GraphPad Prism software.

780 **Materials availability**

781 Plasmids utilized by this study are available from Sigma Aldrich. Mouse lines generated by this
782 study may be available at personal request from the lead contact. No new reagents were
783 created or used by this study.

784

785 **Data and code availability**

786 All data are available in the main text or the Extended Data. Code for RNA sequencing can be
787 retrieved upon request.

Figure Legends

Fig. 1. Hepatic mitochondrial phospholipidome in mouse models of MASLD

(a) A schematic for performing mitochondrial phospholipidomic analyses in liver samples from humans. (b) Representative H&E staining from individuals with healthy or MASH liver. (c) Hepatic mitochondrial CL levels from healthy controls or individuals with MASH (*n*=10 and 16 per group). (d) Hepatic mitochondrial PG levels from healthy controls or individuals with MASH (*n*=10 and 16 per group). (e) Pathway for CL biosynthesis. (f) Representative H&E staining of livers from mice given standard chow or a Western HFD for 16 wks.(g) Representative H&E staining of livers from 20 wk old wildtype or ob/ob mice. (h) Representative Masson's Trichrome staining of livers from mice given standard chow or GAN diet for 30wks. (i) Representative Masson's Trichrome staining of livers from mice injected with vehicle or carbon tetrachloride for 6wks.(j) Representative western blot of OXPHOS subunits and citrate synthase in liver tissues from mice given standard chow or a Western HFD for 16 wks. (k) Representative western blot of OXPHOS subunits and citrate synthase in liver tissues from 20 wk old wildtype or ob/ob mice . (l) Representative western blot of OXPHOS subunits and citrate synthase in liver tissues from mice given standard chow or the GAN diet for 30 wks. (m) Representative western blot of OXPHOS subunits and citrate synthase in liver tissues from mice injected with vehicle or carbon tetrachloride for 6 wks.(n) A heatmap of hepatic mitochondrial phospholipidome of mice given standard chow or HFD for 16 wks. (o) A heatmap of hepatic mitochondrial phospholipidome of 20 wk old wildtype or ob/ob mice. (p) A heatmap of hepatic mitochondrial phospholipidome of mice given standard chow or the GAN diet for 30 wks. (q) A heatmap of hepatic mitochondrial phospholipidome of mice injected with vehicle or carbon tetrachloride for 6 wks. (r) Venn Diagram comparing hepatic mitochondrial phospholipidome from all four models of MASLD: HFD, ob/ob, GAN, or carbon tetrachloride. (s) CLS mRNA levels in livers of mice given standard chow or a Western HFD for 16 wks (*n*=4 per group). (t) CLS mRNA levels in livers from 20 wk old wildtype or ob/ob mice (*n*=6 per group). (u) CLS mRNA levels in livers from mice given

814 standard chow or the GAN diet for 30 wks (*n*=5 per group).(v) CLS mRNA levels in livers from
815 mice injected with vehicle or carbon tetrachloride for 6 wks (*n*=6 and 5 per group). Statistical
816 significance was determined by 2-way ANOVA with a within-row pairwise comparison (c, d, n, o,
817 p, and q) and unpaired, two-sided Student's T test (c and d insert, s, t, u, and v). Measurements
818 were taken from distinct samples for all groups.
819
820 **Fig. 2. Hepatocyte-specific deletion of CLS induces MASLD/MASH**
821 (a) A schematic for hepatocyte-specific deletion of CLS in mice. (b) CLS mRNA levels in livers
822 from control and CLS-LKO mice (*n*=5 and 7 per group). (c) Mitochondrial CL levels in liver from
823 control and CLS-LKO mice (*n*=5 and 6 per group). (d) Body mass of control and CLS-LKO mice
824 (*n*=13 and 11 per group). (e) Body composition of control and CLS-LKO mice (*n*=6 and 7 per
825 group). (f) Liver mass of control and CLS-LKO mice (*n*=10 and 13 per group). (g)
826 Representative H&E staining of livers from control and CLS-LKO mice. (h) Representative
827 Masson's Trichrome staining of livers from control and CLS-LKO mice. (i) An RNAseq-derived
828 heatmap of select genes associated with MASH, liver regeneration, and HCC for control and
829 CLS-LKO mice (*n*=7 and 5 per group). (j) Serum AST for control and CLS-LKO mice (*n*=6 and 7
830 per group). (k) Serum ALT for control and CLS-LKO mice (*n*=6 and 7 per group). (l) mRNA
831 levels of TNFα, TGFβ, IL-12, and MCP1 in livers from control and CLS-LKO mice (*n*=5 and 7
832 per group). (m) Representative image of flow cell population gating for livers from control and
833 CLS-LKO mice (*n*=5 and 7 per group). (n) cDC2 cell population in livers from control and CLS-
834 LKO mice (*n*=5 and 7 per group). (o) F4/80+ cell population in livers from control and CLS-LKO
835 mice (*n*=5 and 7 per group). (p) Ly6C^{hi} inflammatory monocyte population in livers from control
836 and CLS-LKO mice (*n*=5 and 7 per group). (q) MHC-II cell population in control and CLS-LKO
837 livers (*n*=5 and 7 per group). (r) Neutrophil cell population in control and CLS-LKO livers (*n*=5
838 and 7 per group). (s) cDC1 cell population in control and CLS-LKO livers (*n*=5 and 7 per group).
839 All results are from mice fed with standard chow. Statistical significance was determined by 2-

way ANOVA with a within-row pairwise comparison (c and l) and unpaired, two-sided Student's T test (b, d, e, f, i-adjusting for FDR, and j-s). Data represent mean + SEM (b, c, d-f, j-l, and n-s). Measurements taken for b and c were from the same samples. Measurements for d, e, f, g, h, and i were taken from distinct samples. Measurements taken for j, k, m-s were from the same samples. Measurements taken for l were from distinct samples.

Fig. 3. CLS deletion increases mitochondrial respiratory capacity

(a) Glucose tolerance test (IPGTT) of control and CLS-LKO mice fed with standard chow (*n*=6 and 7 per group). (b) Area under the curve for IPGTT. (c) Pyruvate tolerance test (PTT) of control and CLS-LKO mice fed with standard chow (*n*=6 and 8 per group). (d) Area under the curve for PTT. (e) An RNAseq-derived heatmap of genes associated with lipogenesis, VLDL, and β-oxidation for control and CLS-LKO mice (*n*=6 and 5 per group). (f) An RNAseq-derived heatmap of genes associated with components of ETS complex structure and function (*n*=6 and 5 per group). (g) Representative electron microscopy images of liver mitochondria from control and CLS-LKO mice. (h) Representative western blot of whole liver tissue lysate using OXPHOS cocktail and citrate synthase in control and CLS-LKO mice. (i) Ratio of mitochondrial to nuclear DNA in liver tissue of control and CLS-LKO mice (*n*=8 per group). (j) Representative tracing from high-resolution respirometry during maximal respiration using TCA cycle intermediates. (k) JO_2 consumption in isolated liver mitochondria from control and CLS-LKO mice in response to 0.5 mM malate, 5 mM pyruvate, 2.5 mM ADP, 10 mM succinate, and 1.5 µM FCCP (*n*=6 per group). (l) JO_2 consumption in isolated liver mitochondria from control and CLS-LKO mice in response to 0.02 mM palmitoyl-carnitine, 0.5 mM malate, and 2.5 mM ADP (*n*=6 per group). (m) Representative western blot of isolated mitochondria using OXPHOS cocktail in control and CLS-LKO mice. All results are from mice fed with standard chow. Statistical significance was determined by 2-way ANOVA with a within-row pairwise comparison (a, c, k, and l) and unpaired, two-sided Student's T test (b, d, e and f- adjusting for FDRs, and i). Data represent

mean + SEM (a-d, k, and l). Data in box-and-whiskers plot in i represent median with min-to-max. Measurements for a, c, g, and i were taken from distinct samples. Measurements from e and f were from the same samples. Measurements from k, l, and m were taken using the same samples.

Fig. 4. Stable isotope tracing with [U-^{13}C] palmitate and [U-^{13}C] glucose in hepa1-6 cells with or without CLS deletion

(a) Schematic illustration of the labeling process during stable isotope tracing with [U-^{13}C] palmitate or [U-^{13}C] glucose. Blue or green circles represent ^{13}C-labeled carbons, and red circles represent unlabeled ^{12}C carbons. The pathway shows the flow from palmitate to beta-oxidation or glucose through glycolysis to the tricarboxylic acid (TCA) cycle, with key intermediates labeled. (b) Levels of labeled succinate from palmitate tracing in hepa1-6 cells without (shSC) or with CLS deletion (shCLS) (*n*=6 per group). (c) Levels of labeled malate from palmitate tracing in hepa1-6 cells without (shSC) or with CLS deletion (shCLS) (*n*=6 per group). (d) Levels of labeled fumarate from palmitate tracing in hepa1-6 cells without (shSC) or with CLS deletion (shCLS) (*n*=6 per group). (e) Levels of labeled pyruvate from glucose tracing in hepa1-6 cells without (shSC) or with CLS deletion (shCLS) (*n*=6 per group). (f) Levels of labeled acetyl-CoA from glucose tracing in hepa1-6 cells without (shSC) or with CLS deletion (shCLS) (*n*=6 per group). (g) Levels of labeled lactate from glucose tracing in hepa1-6 cells without (shSC) or with CLS deletion (shCLS) (*n*=6 per group). (h) Levels of labeled succinate from glucose tracing in hepa1-6 cells without (shSC) or with CLS deletion (shCLS) (*n*=6 per group). (i) Levels of labeled fumarate from glucose tracing in hepa1-6 cells without (shSC) or with CLS deletion (shCLS) (*n*=6 per group). (j) Levels of labeled citrate from glucose tracing in hepa1-6 cells without (shSC) or with CLS deletion (shCLS) (*n*=6 per group). Statistical significance was determined by unpaired, two-sided Student's T test. Data represent mean $\pm$ SEM. Measurements were taken from the same samples for b-d and a different set of samples for e-j.

Fig. 5. CL deficiency promotes mitochondrial electron leak

(a) Representative electron microscopy images for control and CLS-LKO mice depicting fibrosis with red arrows. (b) mRNA levels of fibrotic markers (Col1a1 and Desmin) in liver tissues from control and CLS-LKO mice (*n*=5 and 7 per group). (c) Levels of cleaved caspase-3 in liver tissues from control and CLS-LKO mice (*n*=4 per group). (d) Levels of cleaved caspase-7 in liver tissues from control and CLS-LKO mice (*n*=4 per group). (e) Levels of mitochondrial cytochrome c in liver tissues of control and CLS-LKO mice (*n*=7 per group). (f) Levels of cytosolic cytochrome c levels in liver tissues of control and CLS-LKO mice (*n*=7 per group). (g) H_2O_2 emission and production in isolated liver mitochondria from control and CLS-LKO mice stimulated with succinate, or succinate, auranofin, and BCNU (*n*=3 and 4 per group). (h) Schematic representation of small unilamellar vesicles (SUVs) containing either cardiolipin (CL) or phosphatidylcholine (PC) to enrich mitochondria with exogenous lipids. (i) H_2O_2 production in liver mitochondria enriched with CL or PC SUVs in control and CLS-LKO mice (*n*=4 per group). All results are from mice fed with standard chow. Statistical significance was determined by 2-way ANOVA with a within-row pairwise comparison (b, g, and i) and unpaired, two-sided Student's T test (c-f). Data represent mean $\pm$ SEM. Measurements from a, b, g, and i are from distinct samples. Measurements from c and d were taken from the same samples. Measurements from e and f were taken from a different set of samples.

Fig. 6. Influence of CL deficiency on respiratory supercomplexes

(a) Representative western blot of respiratory supercomplexes detected using supercomplex antibody cocktail in isolated mitochondria from livers taken from control and CLS-LKO mice. (b) Representative western blot of respiratory supercomplex detected using GRIM19/complex I antibody in isolated mitochondria from livers taken from control and CLS-LKO mice (*n*=4 per group). (c) Quantification of b. (d) Representative western blot of respiratory supercomplex

detected using the NDUFA9/complex I antibody in isolated mitochondria from livers taken from control and CLS-LKO livers (*n*=4 per group). (e) Quantification of d. (f) Representative western blot of respiratory supercomplex detected using the SDHA2/complex II antibody in isolated mitochondria from livers taken from control and CLS LKO livers (*n*=4 per group). Complex II is not thought to form respiratory supercomplexes. (g) Quantification of f. (h) Representative western blot of respiratory supercomplex detected using the UQCRFS1/complex III antibody in isolated mitochondria from livers taken from control and CLS-LKO livers (*n*=4 per group). (i) Quantification of h. (j) Representative western blot of respiratory supercomplex detected using the MTCO1/complex IV antibody in isolated mitochondria from livers taken from control and CLS-LKO livers (*n*=4 per group). (k) Quantification of j. (l) Representative western blot of respiratory supercomplex detected using the ATP5A/complex V antibody in isolated mitochondria from livers taken from control and CLS-LKO livers (*n*=4 per group). (m) Quantification of l. All results are from mice fed with standard chow. Statistical significance was determined by 2-way ANOVA with a within-row pairwise comparison (first panel in c, first panel in e, first panel in i, and first panel in k) and unpaired, two-sided Student's T test (second panel in c, second panel in e, g, second panel in i, second panel in k, and both panels in m). Data represent mean $\pm$ SEM. Measurements from a-m were taken from the same samples.

Fig. 7. CL deficiency disrupts coenzyme Q homeostasis in mice and humans

(a) A schematic for site-specific electron leak. (b) Electron leak at site I_Q in liver mitochondria from control and CLS-LKO mice (*n*=7 per group). (c) Electron leak at site I_F in liver mitochondria from control and CLS-LKO mice (*n*=7 per group. (d) Electron leak at site II_F in liver mitochondria from control or CLS-LKO mice (*n*=7 per group). (e) Electron leak at site III_{Q0} in liver mitochondria from control or CLS-LKO mice (*n*=7 per group). (f) Oxidized coenzyme Q (CoQ) (ubiquinone) can be charged with electrons to become reduced CoQ (ubiquinol). (g) Oxidized CoQ levels in isolated mitochondrial fractions from livers taken from control and CLS-LKO mice (*n*=7 per

944 group). (h) Reduced CoQ levels in isolated mitochondrial fractions from livers taken from control
945 and CLS-LKO livers (*n*=7 per group). (i) CoQ levels in in isolated mitochondria from livers of
946 healthy human controls or patients with advanced steatohepatitis (*n*=10 and 16 per group). (j)
947 Pearson correlation analysis of CL and CoQ levels in human liver samples ($R^2 = 0.64$). Data
948 from b-e,g,h are from mice fed with standard chow. Statistical significance was determined by
949 unpaired two-sided Student's T test (b-e and insert in i) and 2-way ANOVA with a within-row
950 pairwise comparison (g, h, i). Data represent mean $\pm$ SEM (b-e, g, h, i). Measurements from b-e
951 were taken from the same samples. Measurements from g and h were taken from the same
952 samples. Measurements from i and j are from the same samples.

References

1. Younossi, Z.M., *et al.* Global epidemiology of nonalcoholic fatty liver disease—Meta-analytic assessment of prevalence, incidence, and outcomes. *Hepatology* **64**, 73-84 (2015).
2. Miao, L.T., Giovanni; Byrne, Christopher D; Cao, Ying-Ying; Zheng, Ming-Hua. Current status and future trends of the global burden of MASLD. *Trends in Endocrinology & Metabolism* **29**, 1043-2760 (2024).
3. Saito, K., *et al.* Characterization of hepatic lipid profiles in a mouse model with nonalcoholic seatohepatitis and subsequent fibrosis. *Scientific Reports* **5**(2015).
4. John, B.S.S. Nonalcoholic Steatohepatitis (NASH). in *StatPearls* (StatPearls Publishing, Treasure Island, 2023).
5. Vigano, L., Lleo, A. & Aghemo, A. Non-alcoholic fatty liver disease, non-alcoholic steatohepatitis, metabolic syndrome and hepatocellular carcinoma—a composite scenario. *Hepatobiliary Surgery and Nutrition* **7**, 130-133 (2018).
6. Fan, J.-G. & Cao, H.-X. Role of diet and nutritional management in non-alcoholic fatty liver disease. *Gastroenterology and Hepatology* **28**, 87-87 (2013).
7. Gordon, D.L., *et al.* Biomarkers of NAFLD progression: a lipidomics approach to an epidemic. *Journal of Lipid Research* **56**, 722-736 (2015).
8. Fu, S., *et al.* Aberrant lipid metabolism disrupts calcium homeostasis causing liver endoplasmic reticulum stress in obesity. *Nature* **473**, 528-531 (2011).
9. Simoes, I.C.M., Fontes, A., Pinton, P., Zischka, H. & Wieckowski, M.R. Mitochondria in non-alcoholic fatty liver disease. *The International Journal of Biochemistry & Cell Biology* **95**, 93-99 (2018).
10. Leveille, M. & Estall, J.L. Mitochondrial Dysfunction in the Transition from NASH to HCC. *Metabolites* **9**, 233 (2019).
11. Einer, C., *et al.* Mitochondrial adaptation in steatotic mice. *Mitochondrion* **59**, 483-495 (2018).
12. Sunny, N.E., Bril, F. & Cusi, K. Mitochondrial Adaptation in Nonalcoholic Fatty Liver Disease: Novel Mechanisms and Treatment Strategies. *Trends in Endocrinology & Metabolism* **28**(2018).
13. Noureddin, M. & Sanyal, A.J. Pathogenesis of NASH: the Impact of Multiple Pathways. *Current Hepatology Reports* **17**, 350-360 (2018).
14. Pfeiffer, K., *et al.* Cardiolipin stabilizes respiratory chain supercomplexes. *Metabolism and Bioenergetics* **278**, 52873-52880 (2003).
15. Johnson, J.M., *et al.* Targeted overexpression of catalase to mitochondria does not prevent cardioskeletal myopathy in Barth syndrome. *Journal of Molecular and Cellular Cardiology* **121**, 94-102 (2018).
16. Houtkooper, R.H. & Vaz, F.M. Cardiolipin, the heart of mitochondrial metabolism. *Cell. Mol. Life Sci.* **65**, 2493-2506 (2008).
17. Schlame ab, M. & Hostetler, K.Y. Cardiolipin synthase from mammalian mitochondria. *Biochimica et Biophysica Acta (BBA) - Molecular and Cell Biology of Lipids* **1348**, 207-213 (1997).
18. Paradies, G., Paradies, V., Ruggiero, F.M. & Petrosillo, G. Role of Cardiolipin in Mitochondrial Function and Dynamics in Health and Disease: Molecular and Pharmacological Aspects. *Cells* **8**, 728 (2019).
19. Funai, K., Summers, S.A. & Rutter, J. Reign in the membrane: How common lipids govern mitochondrial function. *Current Opinion in Cell Biology* **63**, 162-173 (2020).
20. Jussupow, A., Luca, A.D. & Kaila, V.R. How cardiolipin modulates the dynamics of respiratory complex I. *Science Advances* **5**(2019).

21. Schwall, C.T., Greenwood, V.L. & Alder, N.N. The stability and activity of respiratory Complex II is cardiolipin-dependent. *Biochimica et Biophysica Acta (BBA) - Molecular and Cell Biology of Lipids* **1817**, 1588-1596 (2012).
22. Bazan, S.*, et al.* Cardiolipin-dependent Reconstitution of Respiratory Supercomplexes from Purified Saccharomyces cerevisiae Complexes III and IV*. **288**, 401-411 (2013).
23. Dudek, J.*, et al.* Cardiolipin deficiency affects respiratory chain function and organization in an induced pluripotent stem cell model of Barth syndrome. *Stem Cell Research* **11**, 806-819 (2013).
24. Sustarsic, E.G.*, et al.* Cardiolipin Synthesis in Brown and Beige Fat Mitochondria Is Essential for Systemic Energy Homeostasis. *Cell Metab* **28**, 159-174 (2018).
25. Jiang, F.*, et al.* Absence of cardiolipin in the crd1 null mutant results in decreased mitochondrial membrane potential and reduced mitochondrial function. *Journal of Biological Chemistry* **275**, 22387-22394 (2000).
26. Xu, Y., Sutachan, J.J., Plesken, H., Kelley, R.I. & Schlame, M. Characterization of lymphoblast mitochondria from patients with Barth syndrome. *Laboratory Investigation; a journal of technical methods and pathology* **85**, 823-830 (2005).
27. Hsu, P.*, et al.* Cardiolipin remodeling by TAZ/tafazzin is selectively required for the initiation of mitophagy. *Autophagy* **11**, 643-652 (2015).
28. Le, C.H.*, et al.* Tafazzin deficiency impairs CoA-dependent oxidative metabolism in cardiac mitochondria. *Journal of Biological Chemistry* **295**, 12485-12497 (2020).
29. Heden, T.D.*, et al.* Mitochondrial PE potentiates respiratory enzymes to amplify skeletal muscle aerobic capacity. *Science Advances* **5**, 8352 (2019).
30. Johnson, J.M.P., Alek D; Balderas, Enrique; Sustarsic, Elahu G; Maschek, J Alan; Brothwell, Marisa J; Alejandro, Jara-Ramos; Panic, Vanja; Morgan, Jeffrey T; Villanueva, Claudio J; Sanchez, Alejandro; Rutter, Jared; Lodhi, Irfan J; Cox, James E; Fisher-Wellman, Kelsey H; Chaudhuri, Dipayan; Gerhart-Hines, Zachary; Funai, Katsuhiko. Mitochondrial phosphatidylethanolamine modulates UCP1 to promote brown adipose thermogenesis. *Science Advances* **9**, 7864 (2023).
31. Kartsoli, S., Kostara, C.E., Tsimihodimos, V., Bbairaktari, E.T. & Christodoulou, D.K. Lipidomics in non-alcoholic fatty liver disease. *World Journal of Hepatology* **12**, 436-450 (2020).
32. Ehud Zigmond, C.V. Two Roads Diverge in the Sick Liver, Monocytes Travel Both. *Cell Press* **10**, 1016 (2020).
33. Zahao, X.-A.C., Guang-Mei; Liu, Yong; Chen, Yu-Xin; Wu, Hong-Yan; Chen, Jin; Xiong, Ya-Li; Tian, Chen; Wang, Gui-Yang; Jia, Bei; Xia, Juan; Wang, Jian; Yan, Xiao-Min; Zhang, Zhao-Ping; Huang, Rui; Wu, Chao. Inhibitory effect of silymarin on CCl4-induced liver fibrosis by reducing Ly6Chi monocytes infiltration. *International Journal of Clinical & Experimental Pathology* **10**, 11941-11951 (2017).
34. Daemen, S.G., Anastasiia; Kalugotla, Gowri; He, Li; Chan, Mandy M.; Beals, Joseph W.: Liss, Kim H.; Klein, Samuel; Feldstein, Ariel E.; Finck, Brian N.; Artyomov, Maxim N.; Schilling, Joel D. Dynamic Shifts in the Composition of Resident and Recruited Macrophages Influence Tissue Remodeling in NASH. *Cell Reports* **34**, 108626 (2021).
35. Liyanage, S.E.G., Peter J.; Ribeiro, Joana; Cristante, Enrico; Sampson, Robert D.; Luhmann, Ulrich F.O.; Ali, Robin R.; Bainbridge, James W. Flow cytometric analysis of inflammatory and resident myeloid populations in mouse ocular inflammatory models. *Experimental Eye Research* **151**, 160-170 (2016).
36. Fry, M. & Green, D.E. Cardiolipin requirement for electron transfer in complex I and III of the mitochondrial respiratory chain. *Journal of Biological Chemistry* **256**, 1874-1880 (1981).

37. Paradies, G., Petrosillo, G., Pistolese, M. & Ruggiero, F.M. Reactive oxygen species affect mitochondrial electron transport complex I activity through oxidative cardiolipin damage. *Gene* **286**, 135-141 (2002).
38. Lange, C., Nett, J.H., Trumpower, B.L. & Hunte, C. Specific roles of protein–phospholipid interactions in the yeast cytochrome bc1 complex structure. *The EMBO Journal* **20**, 6591-6600 (2001).
39. Robinson, N.C. Functional binding of cardiolipin to cytochrome c oxidase. *Journal of Bioenergetics and Biomembranes* **25**, 153-163 (1993).
40. Koliaki, C.*, et al.* Adaptation of hepatic mitochondrial function in humans with non-alcoholic fatty liver is lost in steatohepatitis. *Cell Metab* **21**, 739-746 (2015).
41. Siripoksup, P.*, et al.* Sedentary behavior in mice induces metabolic inflexibility by suppressing skeletal muscle pyruvate metabolism. *J Clin Invest* **134**(2024).
42. Drose, S. & Brandt, U. The Mechanism of Mitochondrial Superoxide Production by the Cytochrome bc1 Complex. *Journal of Biological Chemistry* **283**, 21649-21654 (2008).
43. Marra, F. & Svegliati-Baroni, G. Lipotoxicity and the gut-liver axis in NASH pathogenesis. *Hepatology* **68**, 280-295 (2018).
44. Buzzetti, E., Pinzani, M. & Tsochatzis, E.A. The multiple-hit pathogenesis of non-alcoholic fatty liver disease (NAFLD). *Metabolism* **65**, 1038-1048 (2016).
45. Turkseven, S.*, et al.* Mitochondria-targeted antioxidant mitoquinone attenuates liver inflammation and fibrosis in cirrhotic rats. *American Physiological Society* **318**, 298-304 (2020).
46. Karakuzu, O.C., Melissa R.; Liu, Yi; Garsin, Danielle A. Amplex Red Assay for Measuring Hydrogen Peroxide Production from Caenorhabditis elegans. *Bio-protocol* **9**, 3409 (2019).
47. Prola, A.B., Jordan; Vandestienne, Aymeline; Piquereau, Jerome; Denis, Raphael GP; Guyot, Stephane; Chauvin, Hadrien; Mourier, Arnaud; Maurer, Marie; Henry, Celine; Khadhraoui, Nahed; Gallerne, Cindy; Molinie, Thibaut; Courtin, Guillaume; Gressette, Melanie; Solgadi, Audrey; Dumont, Florent; Castel, Julien; Ternacle, Julien; Demarquoy, Jean; Malgoyre, Alexandra; Koulmann, Nathalie; Derumeaux, Genevieve; Giraud, Marie-France; Joubert, Frederic; Veksler, Vladimir; Luquet, Serve; Relaix, Frederic; Tiret, Laurent; Pilot-Storck, Fanny. Cardiolipin content controls mitochondrial coupling and energetic efficiency in muscle. *Science Advances* **7**(2021).
48. Mileykovskaya, E. & Dowhan, W. Cardiolipin-Dependent Formation of Mitochondrial Respiratory Supercomplexes. *Chemistry and Physics of Lipids* **179**, 42-48 (2014).
49. Pennington, E.R., Funai, K., Brown, D.A. & Shaikh, S.R. The role of cardiolipin concentration and acyl chain composition on mitochondrial inner membrane molecular organization and function. *Biochimica et Biophysica Acta (BBA) - Molecular and Cell Biology of Lipids* **1864**, 1039-1052 (2019).
50. Arnarez, C., Marrink, S.J. & Periole, X. Molecular mechanism of cardiolipin-mediated assembly of respiratory chain supercomplexes. *Chemical Science* (2016).
51. Bottinger, L.*, et al.* Phosphatidylethanolamine and Cardiolipin Differentially Affect the Stability of Mitochondrial Respiratory Chain Supercomplexes. *Journal of Molecular Biology* **5**, 677-686 (2012).
52. Dornas, W. & Schuppan, D. Mitochondrial oxidative injury: a key player in nonalcoholic fatty liver disease. *Gastrointestinal and Liver Physiology* **319**, G400-G411 (2020).
53. Gomez, B. & Robinson, N.C. Quantitative Determination of Cardiolipin in Mitochondrial Electron Transferring Complexes by Silicic Acid High-Performance Liquid Chromatography. *Analytical Biochemistry* **267**, 212-216 (1999).
54. Brand, M.D. Mitochondrial generation of superoxide and hydrogen peroxide as the source of mitochondrial redox signaling. *Free Radical Biology and Medicine* **100**, 14-31 (2016).

55. Decker, S.T.F., Katsuhiko. Mitochondrial membrane lipids in the regulation of bioenergetic flux. *Cell Metab* **36**, 1963-1978 (2024).
56. Bessone, F., Razori, M.V. & Roma, M.G. Molecular pathways of nonalcoholic fatty liver disease development and progression. *Cell. Mol. Life Sci.* **76**, 99-128 (2019).
57. Ines C. M. Simoes, R.A., Jose Teixeira, Agnieszka Karkucinska-Wieckowska, Adriana Carvalho, Susana P. Pereira, Rui F. Simoes, Sylwia Szymanska, Michal Dabrowski, Justyna Janikiewicz, Agnieszka Dobrzyn, Paulo J. Oliveira, Yaiza Potes, Mariusz R. Wieckowski. The Alterations of Mitochondrial Function during NAFLD Progression-- An Independent Effect of Mitochondrial ROS Production. *International Journal of Molecular Sciences* **22**, 6848 (2021).
58. Simoes, I.C., Fontes, A., Pinton, P., Zischka, H. & Wieckowski, M.R. Mitochondria in non-alcoholic fatty liver disease. *The International Journal of Biochemistry & Cell Biology* **95**, 93-99 (2017).
59. Goncalves, R.L.S., Schlame, M., Bartelt, A.L., Brand, M.D. & Hotamisligil, G.S. Cardiolipin deficiency in Barth syndrome is not associated with increased superoxide/H2O2 production in heart and skeletal muscle mitochondria. *FEBS Letters* **595**, 415-432 (2021).
60. Xu, Y.*, et al.* Loss of protein association causes cardiolipin degradation in Barth syndrome. *Nature Chemical Biology* **12**, 641-647 (2016).
61. Simoes, I.C.A., Ricardo; Teixeira, Jose; Karkucinska-Wieckowska, Agnieszka; Carvalho, Adriana; Pereira, Susana P.; Simoes, Rui F.; Szymanska Sylwia; Dabrowski, Michal; Janikiewicz, Justyna; Dobrzyn, Agnieszka; Oliveira, Paulo J.; Potes, Yaiza; Wieckowski, Mariusz R. . The Alterations of Mitochondrial Function during NAFLD Progression-- An Independent Effect of Mitochondrial ROS Production. *International Journal of Molecular Sciences* **22**, 6848 (2021).
62. Bazan, S.*, et al.* Cardiolipin-dependent Reconstitution of Respiratory Supercomplexes from Purified Saccharomyces cerevisiae Complexes III and IV*. *Journal of Biological Chemistry* **288**, 401-411 (2013).
63. Miwa, S.*, et al.* Carboxylesterase converts Amplex red to resorufin: Implications for mitochondrial H2O2 release assays. *Free Radical Biology and Medicine* **90**(2016).

Acknowledgements

This research was supported by National Institutes of Health (NIH) grants DK127979, GM144613, DK107397, AG074535 (to KF); DK127603 (to AMP), DK130555 (to ADP); HL170575, DK112826 (to WLH); GM151245 (to SMN), CA278803 (to KHF-W); DK128819, DK115991 (to PNM); CA222570 (to KJE); CA272529, DK130296, DK131609 (to SAS); DK091317 (to MJB, TST, STD), by American Heart Association grants 915674 (to PS) and 19PRE34380991 (to JMJ), by European Research Council (ERC) under the European Union's Horizon 2020 Research and Innovation Programme (Starting Grant aCROBAT agreement no. 639382 to ZGH), by Damon Runyon Cancer Research Foundation (Damon Runyon-Rachleff Innovation Award DR 61-20 to KJE), by a pilot grant from Washington University DRC P30 DK020579, and by the Huntsman Cancer Foundation. The University of Utah Metabolomics Core Facility is supported by NIH S10 OD016232, S10 OD021505, and U54 DK110858. Research reported in this publication utilized the Huntsman Cancer Institute Biorepository and Molecular Pathology Shared Resources supported by NCI/NIH P30 CA042014. We thank Nikita Abraham and Diana Lim (University of Utah Molecular Medicine Program) for assistance with figures.

Contributions

Conception: M.J.B., K.F., M.P., S.A.S., and T.S.T. Experimental design: M.J.B., K.F., P.S., F.M.F., Z.G.-H., and W.L.H. Investigation: M.J.B., K.F., G.C., J.A.M., A.M.P., A.D.P., L.W., T.B.B., J.L.S., P.S., Q.J.P., J.M.J., A.P., S.A.P., P.N.M., G.L.H., A.M.M., S.W., E.R.M., K.E.A., L.S.N., R.H.C., and S.T.D. Methodology: J.A.M., Q.J.P., J.M.J., F.M.F., Z.G.-H., A.P., S.A.P., P.N.M., G.L.H., J.L.C., S.M.N., D.S.L., K.H.F.-W., J.E.C., and L.S.N. Resources: F.M.F., Z.G.-H., W.L.H., K.J.E., and S.A.S. Formal analysis: M.J.B., K.F., G.C., J.A.M., A.D.P., L.W., R.H.C., J.L.C., and S.A.P. Writing: M.J.B. and K.F. All authors read and approved the paper.

Corresponding Author

Correspondance to Katsuhiko Funai

E-mail: kfunai@health.utah.edu

Ethics Declarations

Competing Interests

The authors declare no competing interests.

Figure 1.

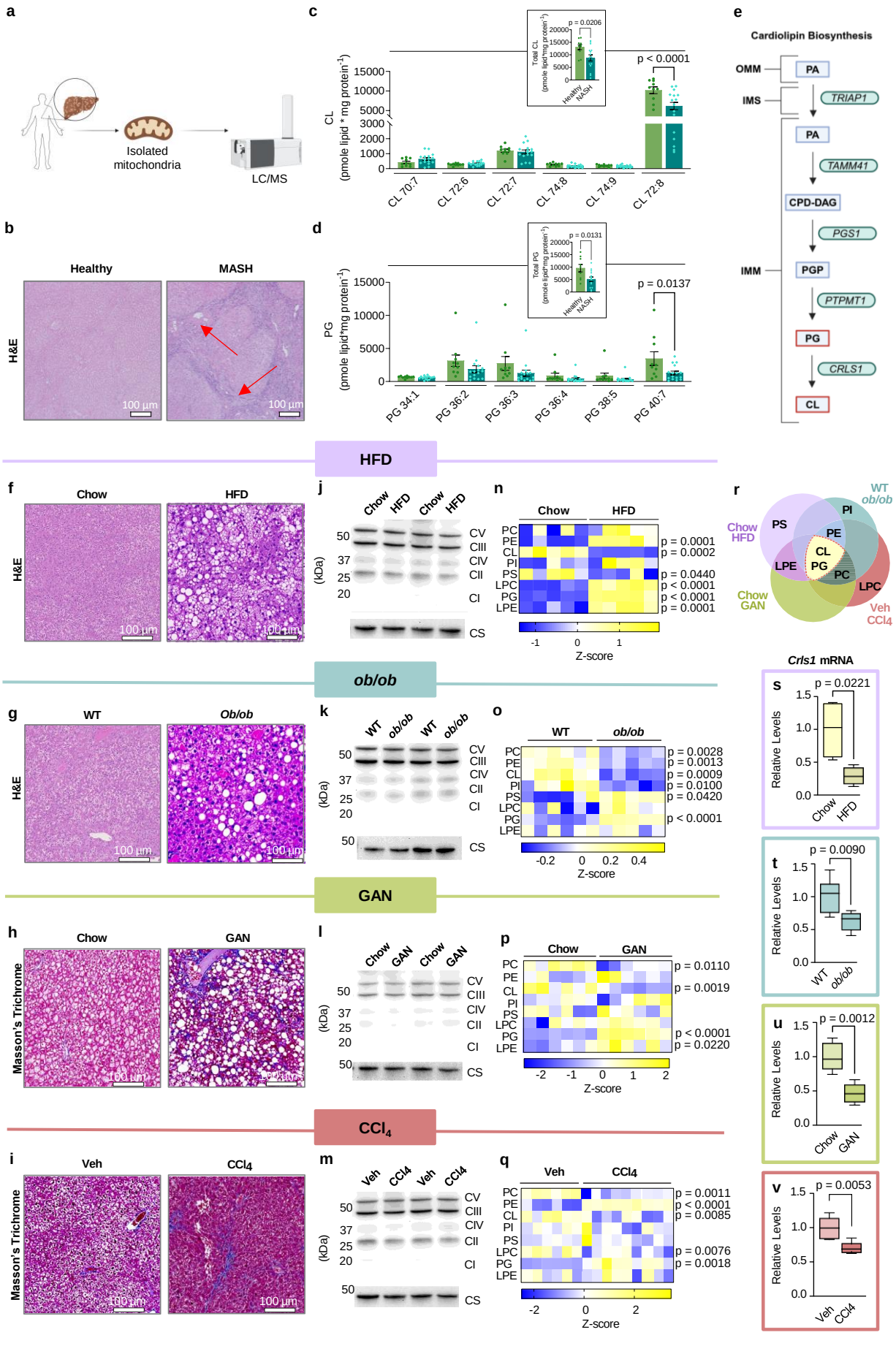

Figure 2.

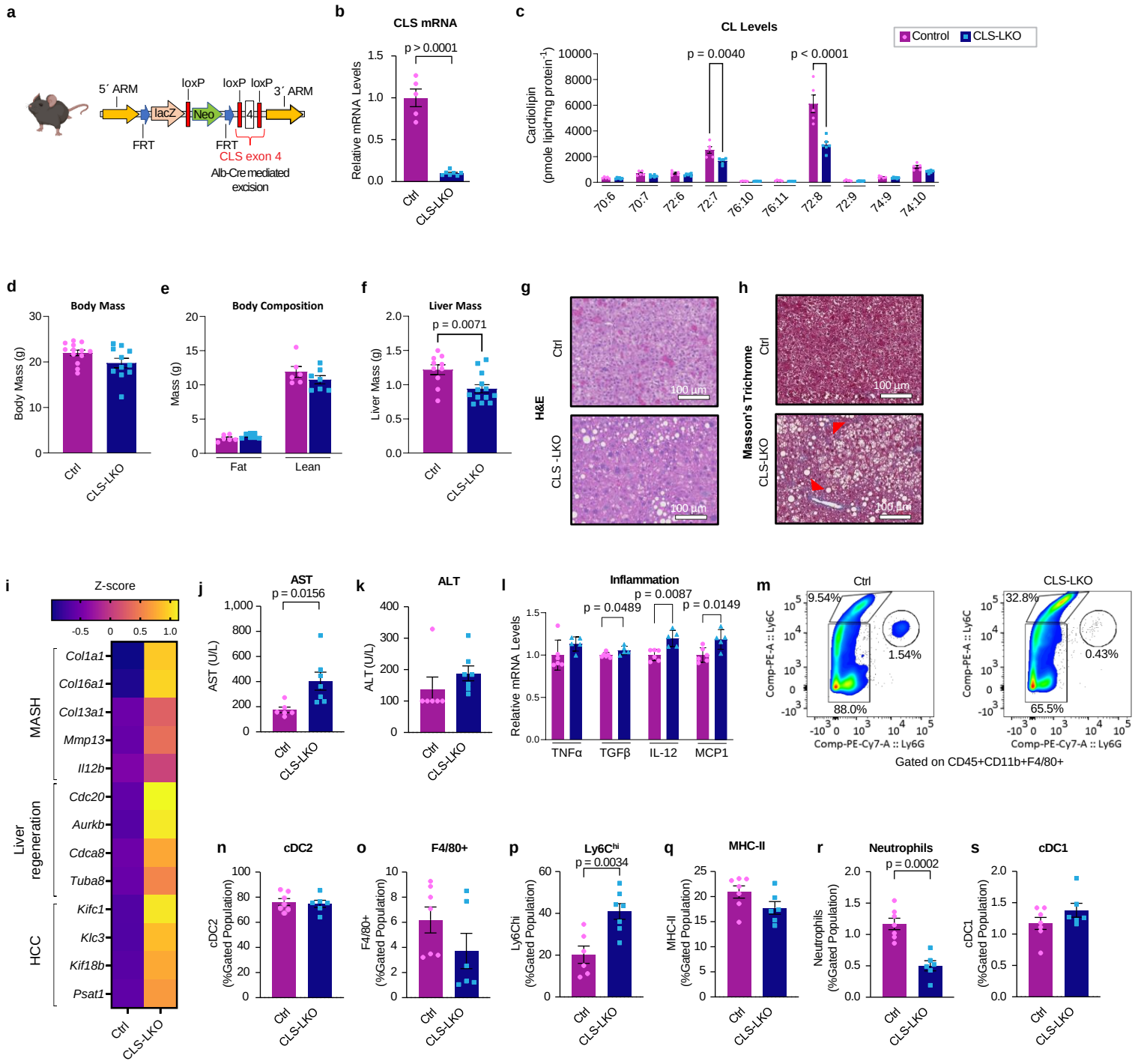

Figure 3.

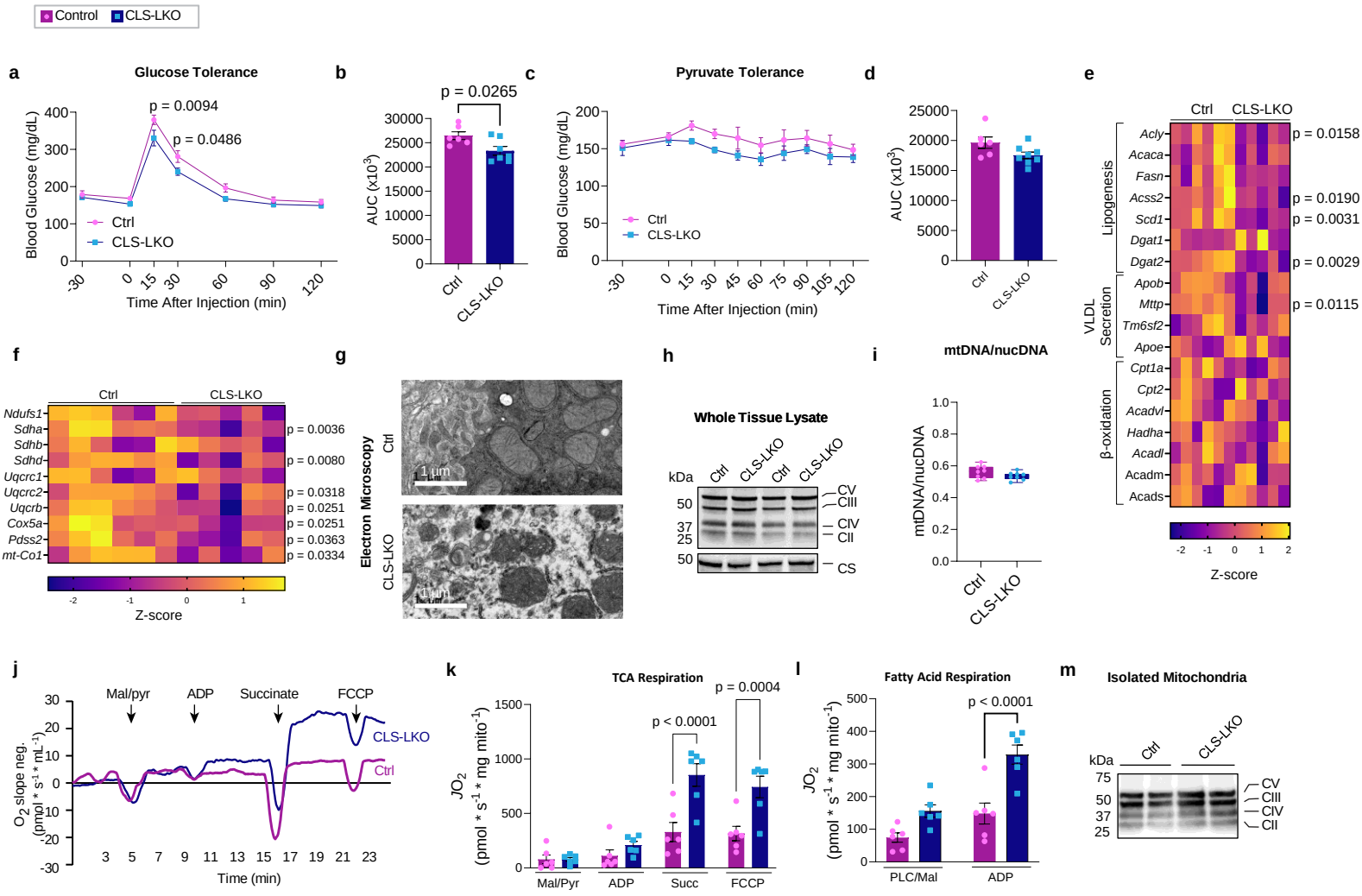

Figure 4.

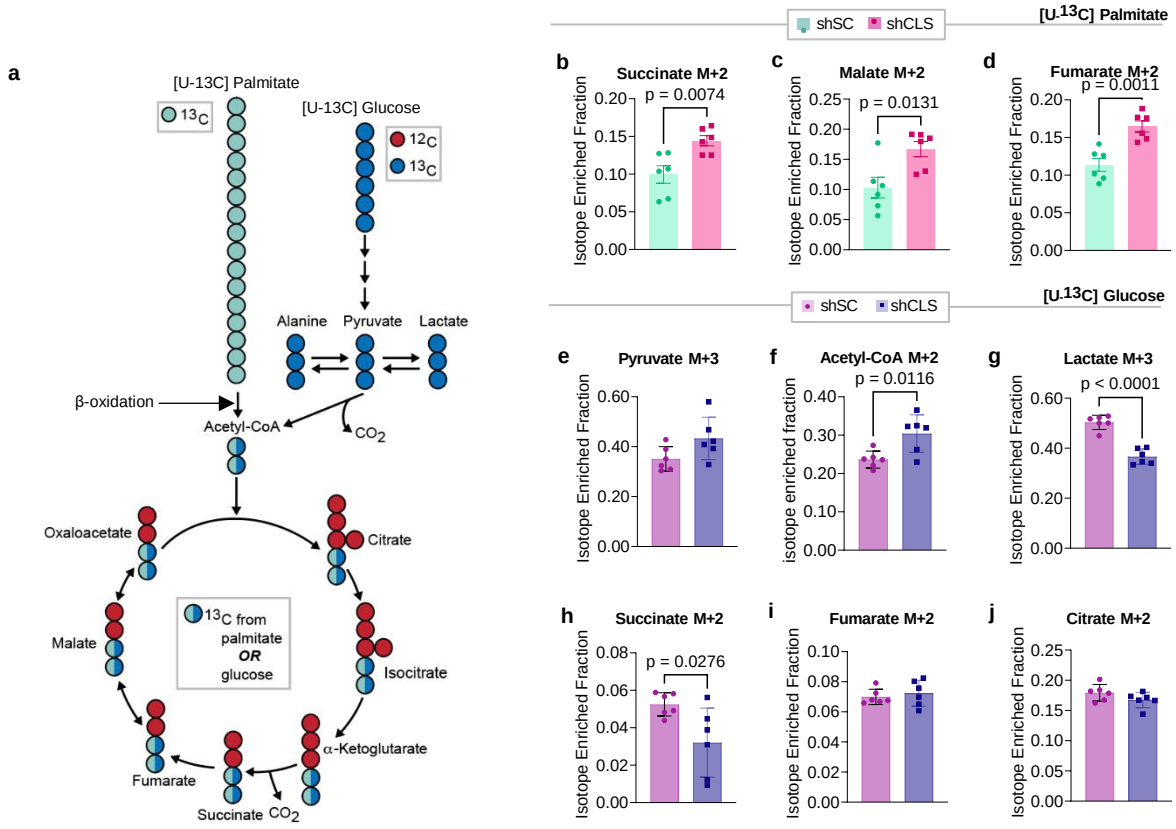

Figure 5.

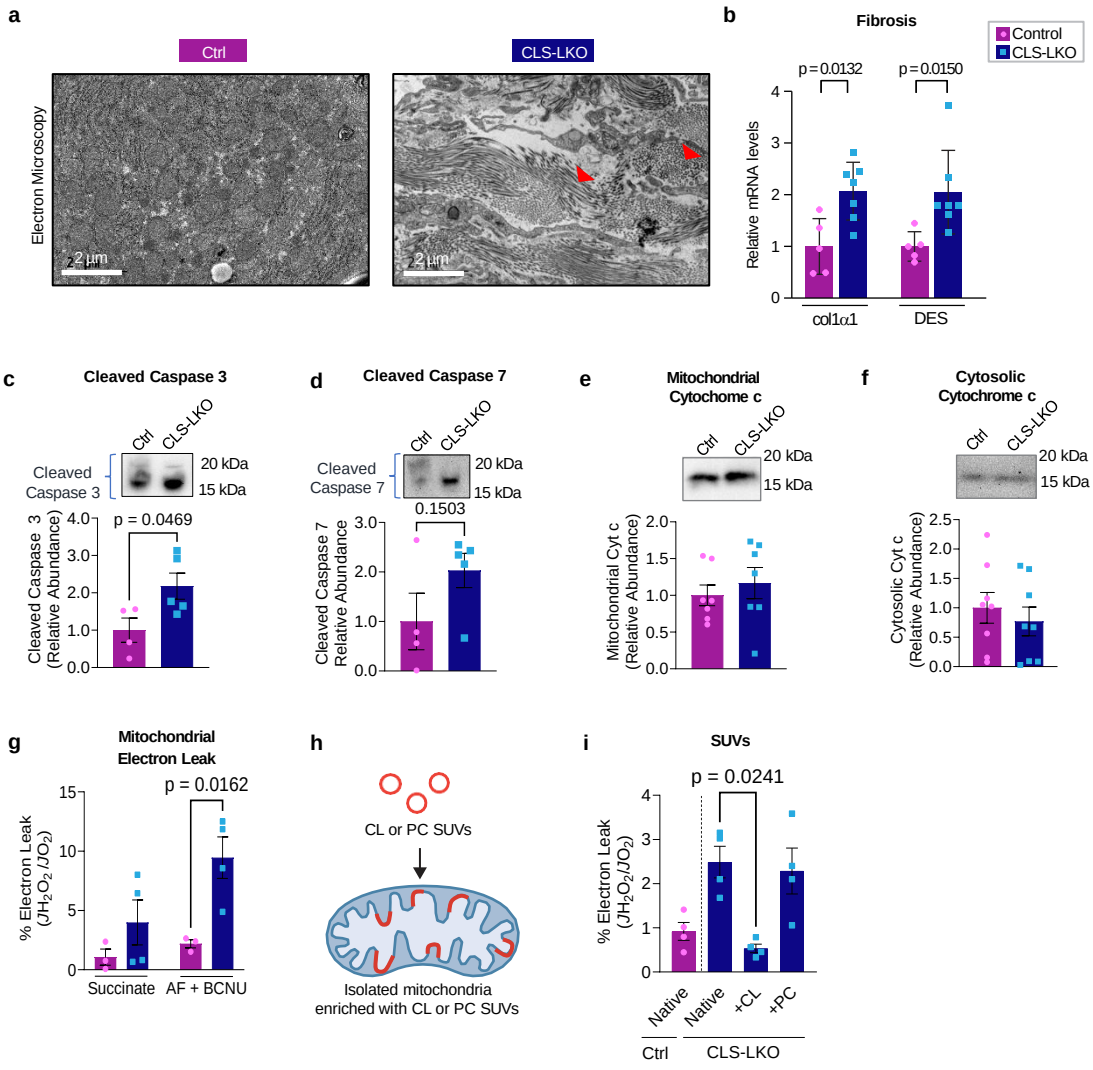

Figure 6.

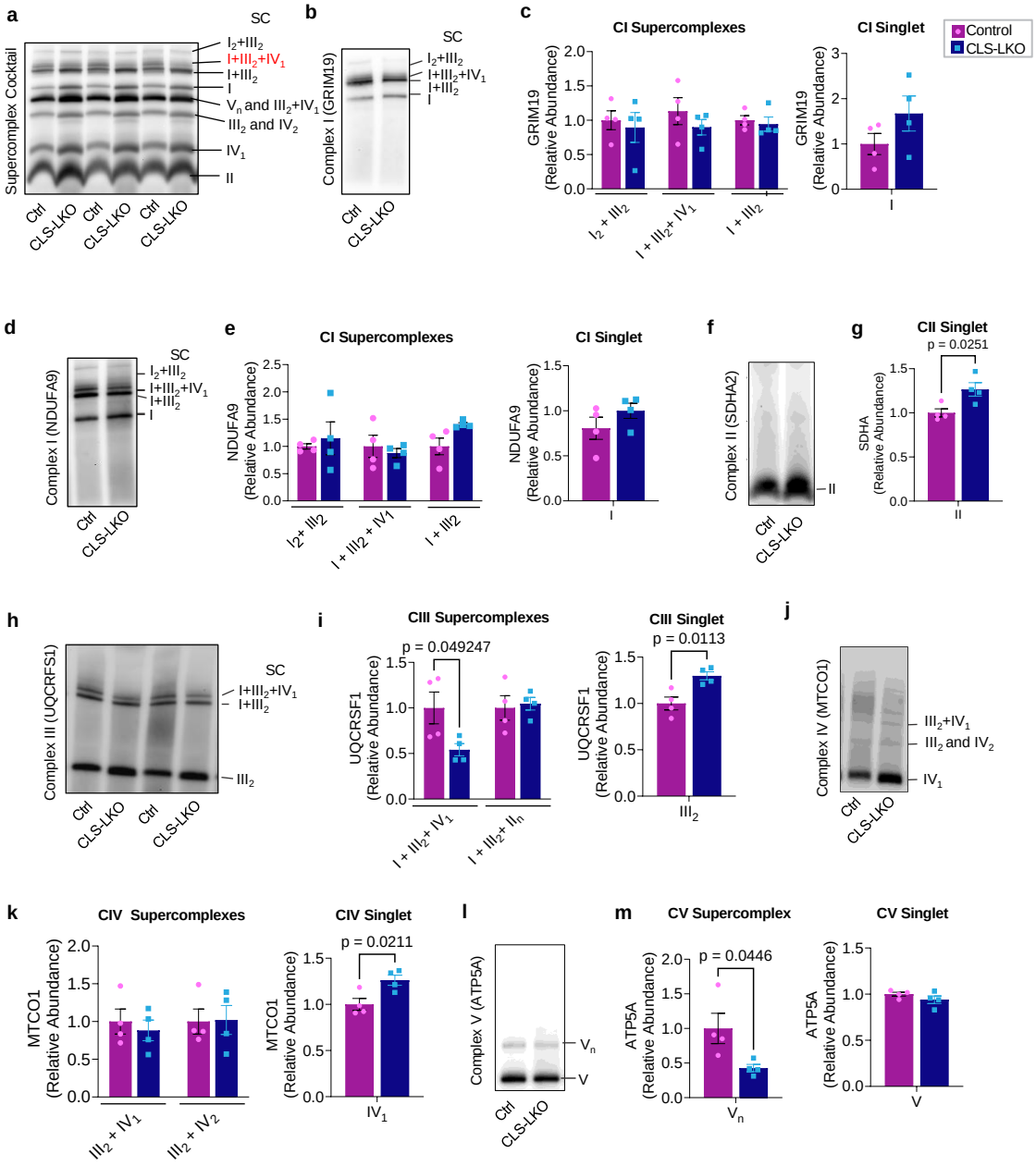

Figure 7

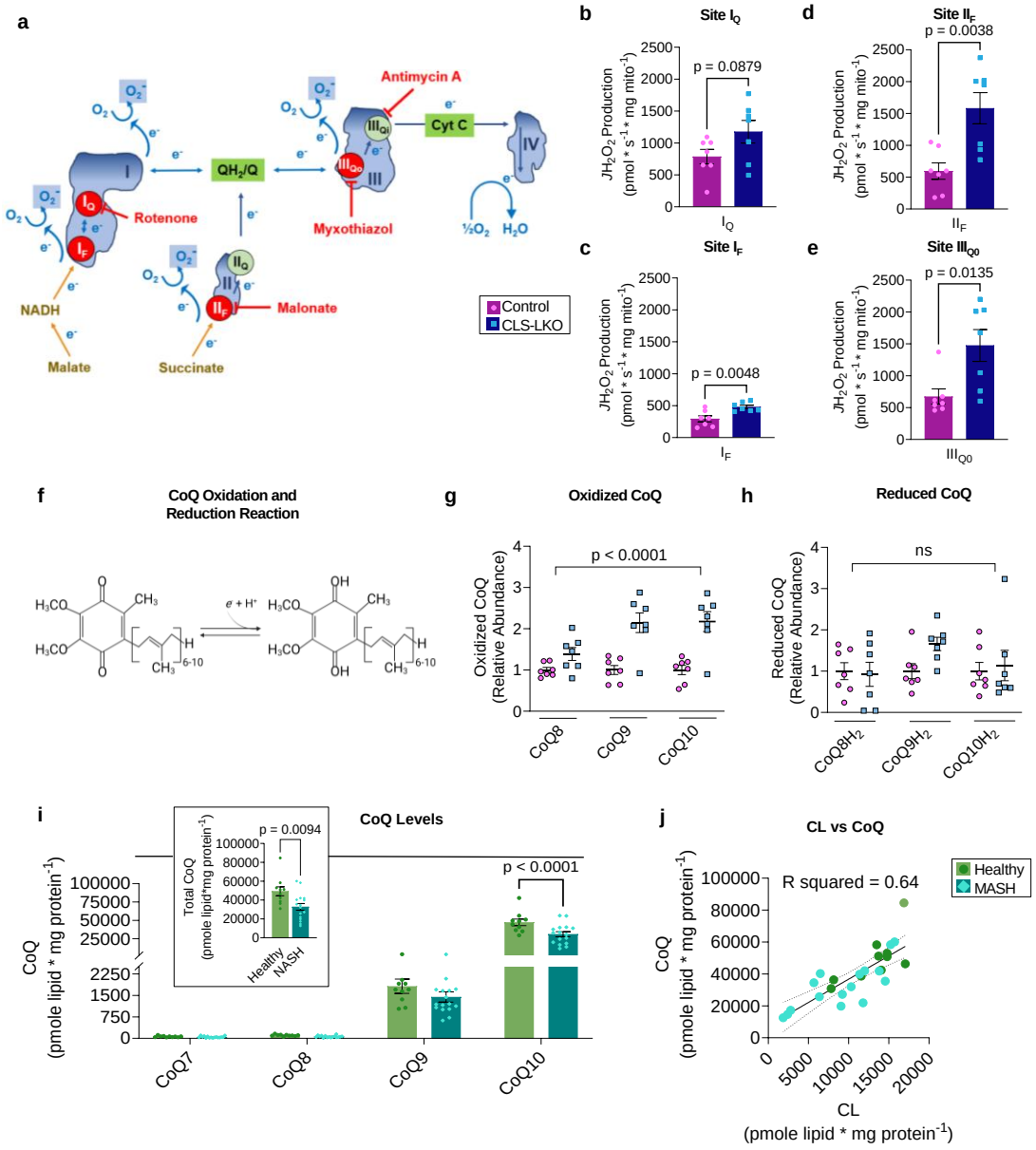

Extended Data Figure Legends

Extended Data Fig. 1. Mitochondrial phospholipidome from Figure 1j,k.

(a) Abundance of mitochondrial CL in liver of mice fed with standard chow or HFD for 16 wks (*n*=5 per group). (b) Abundance of mitochondrial PC in liver of mice fed standard chow or HFD for 16 wks (*n*=5 per group). (c) Abundance of mitochondrial PE in liver of mice fed with standard chow or HFD for 16 wks (*n*=5 per group). (d) Abundance of mitochondrial PI in liver of mice fed with standard chow or HFD for 16 wks (*n*=5 per group). (e) Abundance of mitochondrial PS in liver of mice fed with standard chow or HFD for 16 wks (*n*=5 per group). (f) Abundance of mitochondrial LPC in liver of mice fed with standard chow or HFD for 16 wks (*n*=5 per group). (g) Abundance of mitochondrial PG in liver of mice fed with standard chow or HFD for 16 wks (*n*=5 per group). (h) Abundance of mitochondrial LPE in liver of mice fed with standard chow or HFD for 16 wks (*n*=5 per group). (i) Abundance of mitochondrial CL in liver from wildtype or leptin-deficient mice, 30 wks old (*n*=6 per group). (j) Abundance of mitochondrial PC in liver from wildtype or leptin-deficient mice, 30 wks old (*n*=6 per group). (k) Abundance of mitochondrial PE in liver from wildtype or leptin-deficient mice, 30 wks old (*n*=6 per group). (l) Abundance of mitochondrial PI in liver from wildtype or leptin-deficient mice, 30 wks old (*n*=6 per group). (m) Abundance of mitochondrial PS in liver from wildtype or leptin-deficient mice, 30 wks old (*n*=6 per group). (n) Abundance of mitochondrial LPC in liver from wildtype or leptin-deficient mice, 30 wks old (*n*=6 per group). (o) Abundance of mitochondrial PG in liver from wildtype or leptin-deficient mice, 30 wks old (*n*=6 per group). (p) Abundance of mitochondrial LPE in liver from wildtype or leptin-deficient mice, 30 wks old (*n*=6 per group). Statistical significance was determined by 2-way ANOVA with a within-row pairwise comparison. Data represent mean ± SEM. Measurements taken from a-h were taken from the same samples. Measurements from i-p were taken from the same samples.

Extended Data Fig. 2. Mitochondrial phospholipidome from Figure 1l,m.

(a) Abundance of mitochondrial CL in livers from mice injected with corn oil or carbon tetrachloride for 10 wks (*n*=5 and 7 per group). (b) Abundance of mitochondrial PC in livers from mice injected with corn oil or carbon tetrachloride for 10 wks (*n*=5 and 7 per group). (c) Abundance of mitochondrial PE in livers from mice injected with corn oil or carbon tetrachloride for 10 wks (*n*=5 and 7 per group). (d) Abundance of mitochondrial PI in livers from mice injected with corn oil or carbon tetrachloride for 10 wks (*n*=5 and 7 per group). (e) Abundance of mitochondrial PS in livers from mice injected with corn oil or carbon tetrachloride for 10 wks (*n*=5 and 7 per group). (f) Abundance of mitochondrial LPC in livers from mice injected with corn oil or carbon tetrachloride for 10 wks (*n*=5 and 7 per group). (g) Abundance of mitochondrial PG in livers from mice injected with corn oil or carbon tetrachloride for 10 wks (*n*=5 and 7 per group). (h) Abundance of mitochondrial LPE in livers from mice injected with corn oil or carbon tetrachloride for 10 wks (*n*=5 and 7 per group). (i) Abundance of mitochondrial CL in livers from mice fed standard chow or Gubra-Amylin MASH diet for 30 wks (*n*=6 per group). (j) Abundance of mitochondrial PC in livers from mice fed standard chow or Gubra-Amylin MASH diet for 30 wks (*n*=6 per group). (k) Abundance of mitochondrial PE in livers from mice fed standard chow or Gubra-Amylin MASH diet for 30 wks (*n*=6 per group). (l) Abundance of mitochondrial PI in livers from mice fed standard chow or Gubra-Amylin MASH diet for 30 wks (*n*=6 per group). (m) Abundance of mitochondrial PS in livers from mice fed standard chow or Gubra-Amylin MASH diet for 30 wks (*n*=6 per group). (n) Abundance of mitochondrial LPC in livers from mice fed standard chow or Gubra-Amylin MASH diet for 30 wks (*n*=6 per group). (o) Abundance of mitochondrial PG in livers from mice fed standard chow or Gubra-Amylin MASH diet for 30 wks (*n*=6 per group). (p) Abundance of mitochondrial LPE in livers from mice fed standard chow or Gubra-Amylin MASH diet for 30 wks (*n*=6 per group). Statistical significance was determined by 2-way ANOVA with a within-row pairwise comparison. Data represent mean $\pm$ SEM. Measurements from a-h were taken from the same samples. Measurements from i-p were taken from the same samples.

Extended Data Fig. 3. Mitochondrial phospholipidome from standard chow or high-fat diet fed control and CLS-LKO livers.

(a) Abundance of mitochondrial PC in liver from control or CLS-LKO mice with standard chow, 8 wks old (*n*=5 and 6 per group). (b) Abundance of mitochondrial PE in liver from control or CLS-LKO mice fed with standard chow, 8 wks old (*n*=5 and 6 per group). (c) Abundance of mitochondrial PI in liver from control or CLS-LKO mice fed with standard chow, 8 wks old (*n*=5 and 6 per group). (d) Abundance of mitochondrial PS in liver from control or CLS-LKO mice fed with standard chow, 8 wks old (*n*=5 and 6 per group). (e) Abundance of mitochondrial LPC in liver from control or CLS-LKO mice fed with standard chow, 8 wks old (*n*=5 and 6 per group). (f) Abundance of mitochondrial PG in liver from control or CLS-LKO mice fed with standard chow, 8 wks old (*n*=5 and 6 per group). (g) Abundance of mitochondrial LPE in liver from control or CLS-LKO mice fed with standard chow, 8 wks old (*n*=5 and 6 per group). (h) Abundance of mitochondrial CL in liver from control or CLS-LKO mice fed a high-fat diet for 8 wks (*n*=11 and 12 per group). (i) Abundance of mitochondrial PC in liver from control or CLS-LKO mice fed a high-fat diet for 8 wks (*n*=11 and 12 per group). (j) Abundance of mitochondrial PE in liver from control or CLS-LKO mice fed a high-fat diet for 8 wks (*n*=11 and 12 per group). (k) Abundance of mitochondrial PI in liver from control or CLS-LKO mice fed a high-fat diet for 8 wks (*n*=11 and 12 per group). (l) Abundance of mitochondrial PS in liver from control or CLS-LKO mice fed a high-fat diet for 8 wks (*n*=11 and 12 per group). (m) Abundance of mitochondrial LPC in liver from control or CLS-LKO mice fed a high fat diet for 8 wks (*n*=11 and 12 per group). (n) Abundance of mitochondrial PG in liver from control or CLS-LKO mice fed a high-fat diet for 8 wks (*n*=11 and 12 per group). (o) Abundance of mitochondrial LPE in liver from control or CLS-LKO mice fed a high fat diet for 8 wks (*n*=11 and 12 per group). Statistical significance was determined by 2-way ANOVA with a within-row pairwise comparison. Data represent mean ±

SEM. Measurements from a-g were taken from the same samples. Measurements from h-o were taken from the same samples.

Extended Data Fig. 4. Additional histological and transcriptomic data from control and CLS-LKO mice.

(a) Representative H&E staining of livers from control and CLS-LKO mice fed a HFD for 8 wks. (b) Representative Masson's Trichrome staining of livers from control and CLS-LKO mice fed a HFD for 8 wks. (c) Volcano plot of differentially expressed genes in livers taken from control and CLS-LKO mice fed with standard chow (*n*=5 and 7 per group). (d) Pathway analysis of transcriptomic data in livers taken control and CLS-LKO mice fed with standard chow (*n*=5 and 7 per group). Pathway analysis was performed using the Reactome Pathway Database. Measurements from a and b were taken from distinct samples. Measurements from c and d were taken from the same samples.

Extended Data Fig. 5. Additional metabolic, mitochondrial, and fluxomic phenotyping data with CLS deletion.

(a) mRNA levels of lipogenic genes in livers from control and CLS-LKO mice fed with standard chow (*n*=6 and 7 per group). (b) Serum triglycerides for control and CLS-LKO mice fed with standard chow (*n*=6 and 7 per group). (c) JO_2 consumption in isolated liver mitochondria from control or CLS-LKO mice fed a HFD for 8 wks in response to 0.5 mM malate, 5 mM pyruvate, 2.5 mM ADP, 10 mM succinate, and 1.5 μM FCCP (*n*=11 and 12 per group). (d) JO_2 consumption in isolated liver mitochondria from control or CLS-LKO mice fed a HFD for 8 wks in response to 0.02 mM palmitoyl-carnitine, 0.5 mM malate, and 2.5 mM ADP (*n*=7 per group). (e) Levels of labeled glycine from glucose tracing in hepa1-6 cells without (shSC) or with CLS deletion (shSLC) (*n*=6 per group). (f) Levels of labeled aspartate from glucose tracing in hepa1-6 cells without (shSC) or with CLS deletion (shSLC) (*n*=6 per group). (g) Levels of labeled 3-

phosphoglyceric acid from glucose tracing in hepa1-6 cells without (shSC) or with CLS deletion (shSLC) (*n*=6 per group). (h) Levels of labeled alanine from glucose tracing in hepa1-6 cells without (shSC) or with CLS deletion (shSLC) (*n*=6 per group). (i) Levels of labeled malate from glucose tracing in hepa1-6 cells without (shSC) or with CLS deletion (shSLC) (*n*=6 per group). Statistical significance was determined by 2-way ANOVA with a within-row pairwise comparison (a, c, and d) and unpaired Student's T test (b, and e-i). Data represent mean ± SEM. Measurements from a and b were taken from distinct samples. Measurements from c and d were taken from the same samples. Measurements from e-i were taken from the same samples.

Extended Data Fig. 6. Additional mitochondrial phenotyping data with CLS deletion.

(a) Levels of mitochondrial cytochrome c in livers of control and CLS-LKO mice fed a HFD for 8 wks (*n*=6 per group). (b) Levels of cytosolic cytochrome c in livers of control and CLS-LKO mice fed a HFD for 8 wks (*n*=6 per group). (c) H_2O_2 emission and production in isolated liver mitochondria from control or CLS-LKO mice fed a HFD for 8 wks, stimulated with succinate, or succinate and auranofin and BCNU (*n*=9 and 8 per group). (d) H_2O_2 emission and production in isolated liver mitochondria from hepa1-6 cells without (shSC) or with CLS deletion (shSLC), stimulated with succinate, or succinate and auranofin and BCNU (*n*=3 per group). (e) Electron leak of liver mitochondria from control mice fused with SUVs (*n*=4 per group). Statistical significance was determined by 2-way ANOVA with a within-row pairwise comparison (c, d, and e) and unpaired Student's T test (a and b). Measurements from a and b were taken from the same samples. Measurements from c, d, and e were taken from distinct samples.

Extended Data Fig. 7. Additional data on coenzyme Q

(a) Total CoQ_8 levels in whole liver tissue from control and CLS-LKO mice (*n*=7 per group). (b) Total CoQ_9 levels in whole liver tissue from control and CLS-LKO mice (*n*=7 per group). (c) Total CoQ_{10} levels in whole liver tissue from control and CLS-LKO mice (*n*=7 per group). (d)

Oxidized CoQ_8 levels in whole liver tissue from control and CLS-LKO mice (*n*=7 per group). (e) Reduced CoQ_8 levels in whole liver tissue from control and CLS-LKO mice (*n*=7 per group). (f) Oxidized CoQ_9 levels in whole liver tissue from control and CLS-LKO mice (n=7 per group). (g) Reduced CoQ_9 levels in whole liver tissue from control and CLS-LKO mice (n=7 per group). (h) Oxidized CoQ_{10} levels in whole liver tissue from control and CLS-LKO mice (*n*=7 per group). (i) Reduced CoQ_{10} levels in whole liver tissue from control and CLS-LKO mice (*n*=7 per group). (j) Oxidized CoQ_8 levels in isolated mitochondria from control and CLS-LKO mice (*n*=7 per group). (k) Reduced CoQ_8 levels in isolated mitochondria from control and CLS-LKO mice (*n*=7 per group). (l) Oxidized CoQ_9 levels in isolated mitochondria from control and CLS-LKO mice (*n*=7 per group). (m) Reduced CoQ_9 levels in isolated mitochondria from control and CLS-LKO mice (*n*=7 per group). (n) Oxidized CoQ_{10} levels in isolated mitochondria from control and CLS-LKO mice (*n*=7 per group). (o) Reduced CoQ_{10} levels in isolated mitochondria from control and CLS-LKO mice (*n*=7 per group). Statistical significance was determined by unpaired Student's T test. Data represent mean $\pm$ SEM. Measurements from a-c were taken from the same samples. Measurements from d-i and j-o were taken from the same samples.

Extended Data Figure 1.

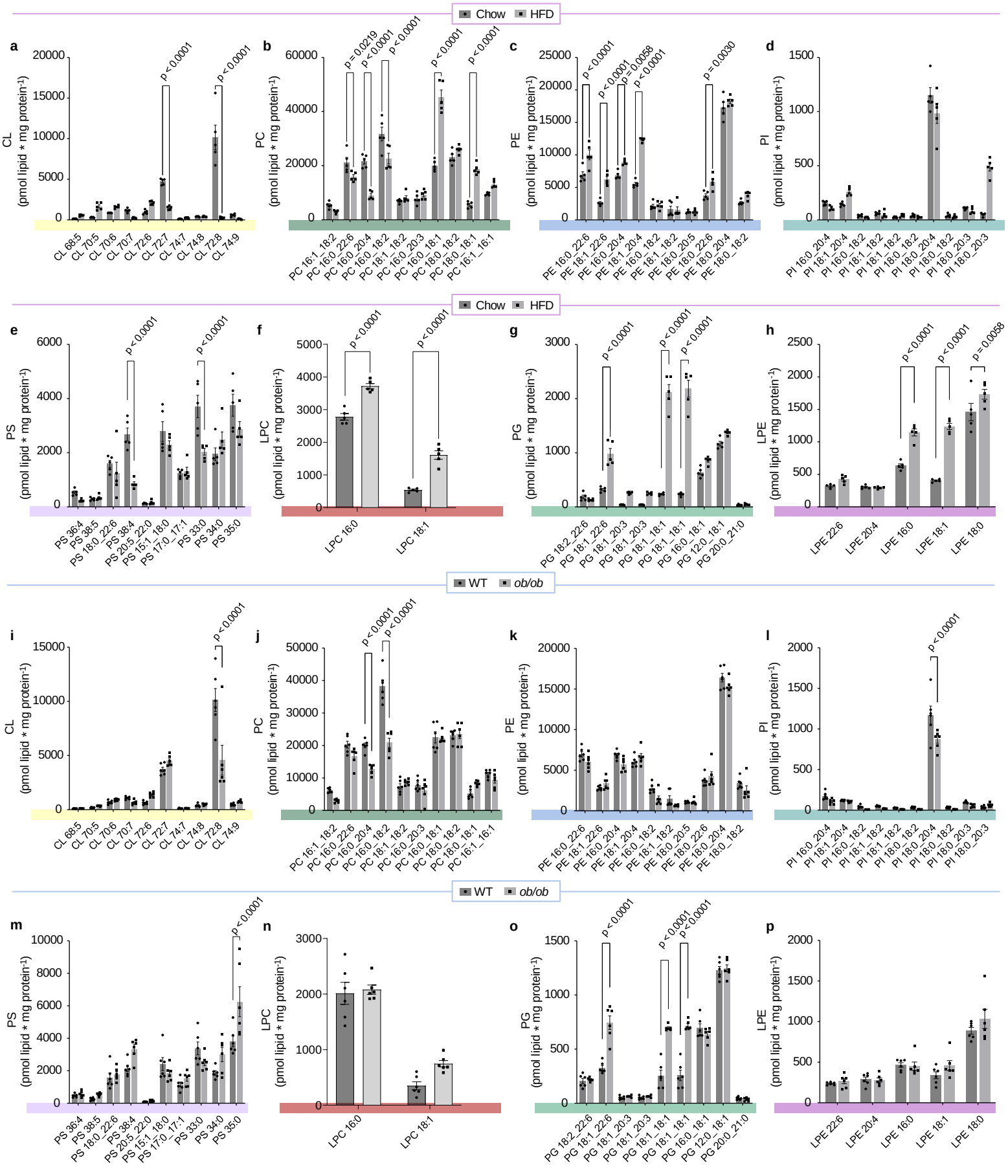

Extended Data Figure 2.

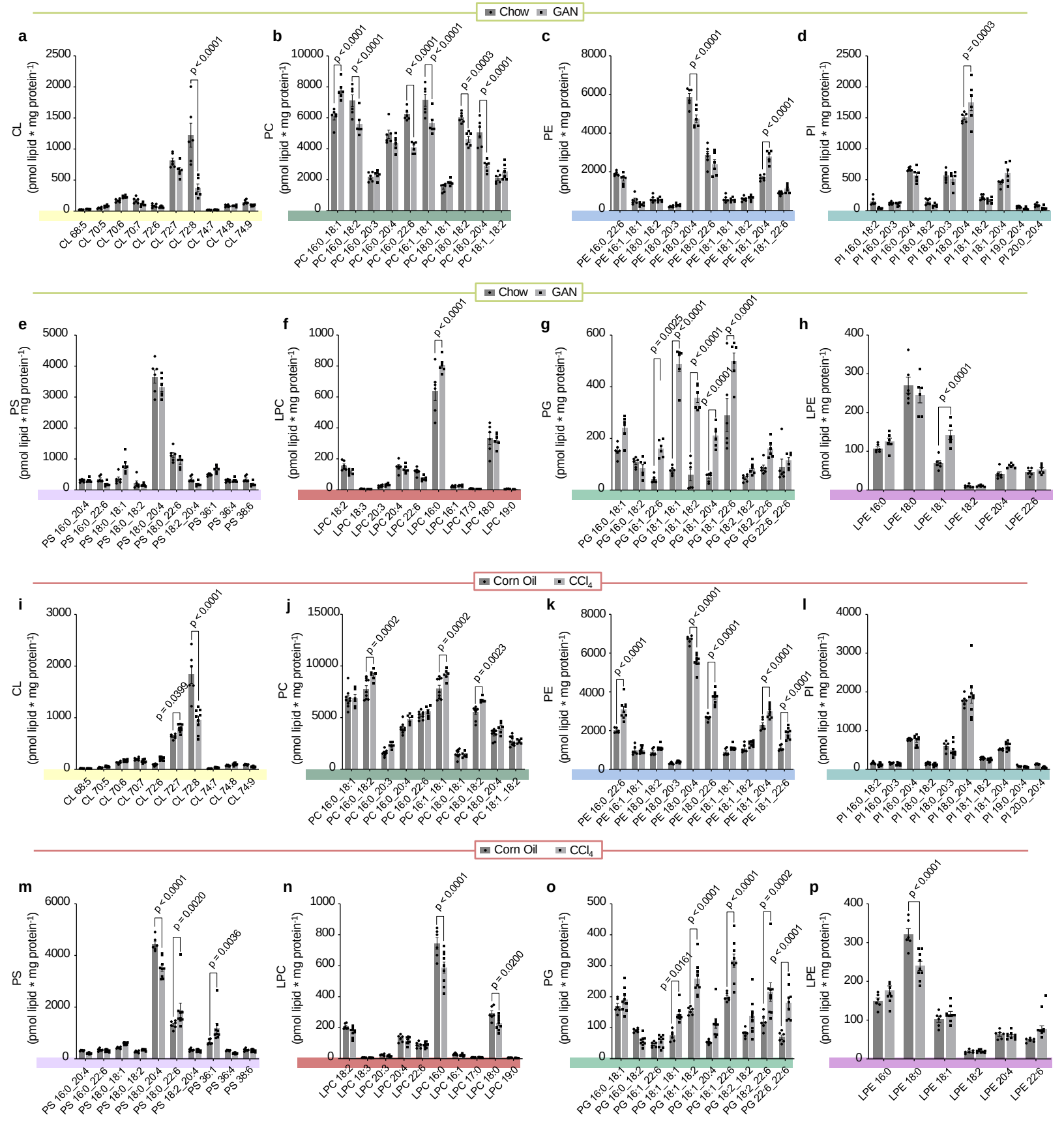

Extended Data Figure 3.

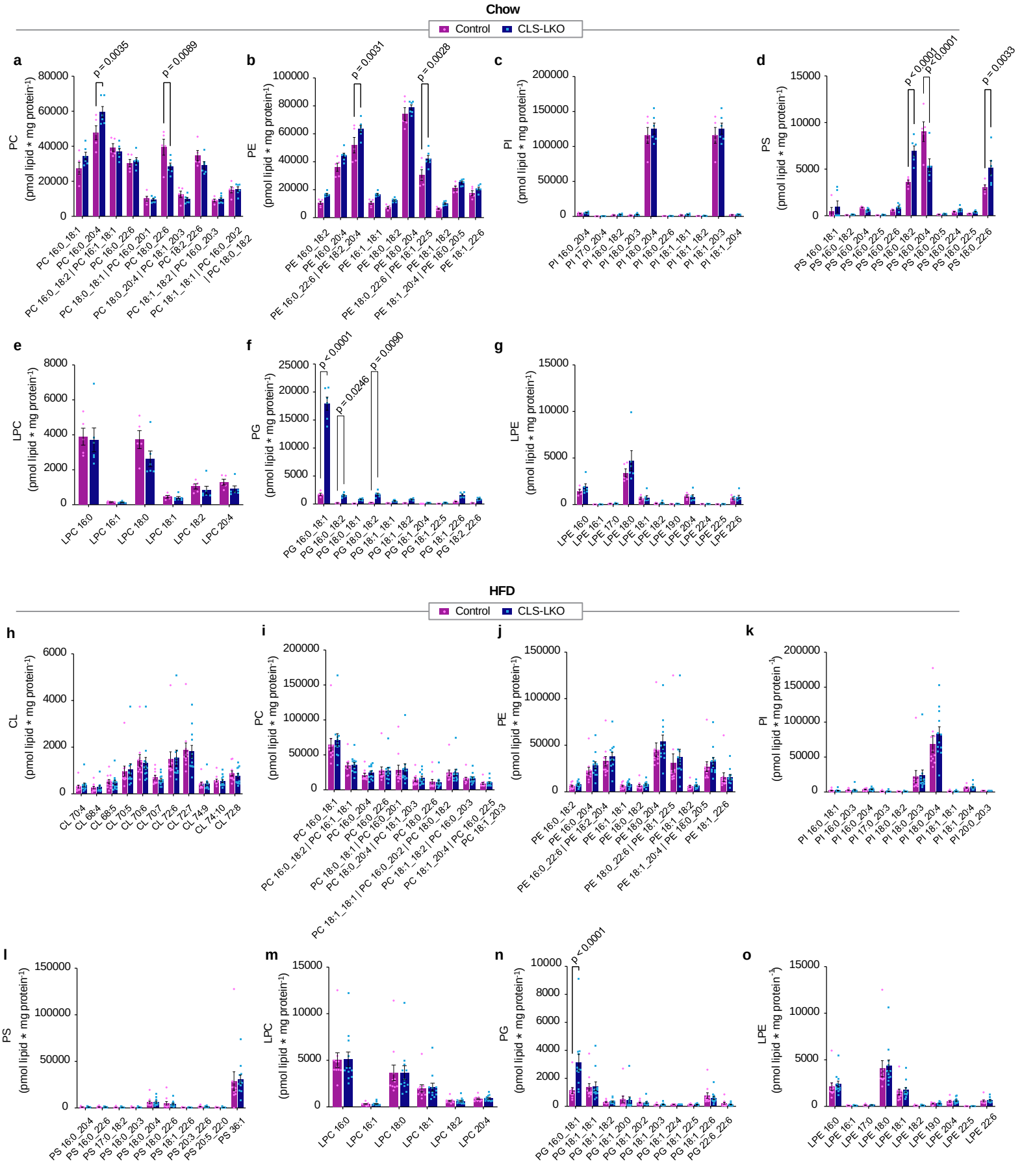

Extended Data Figure 4.

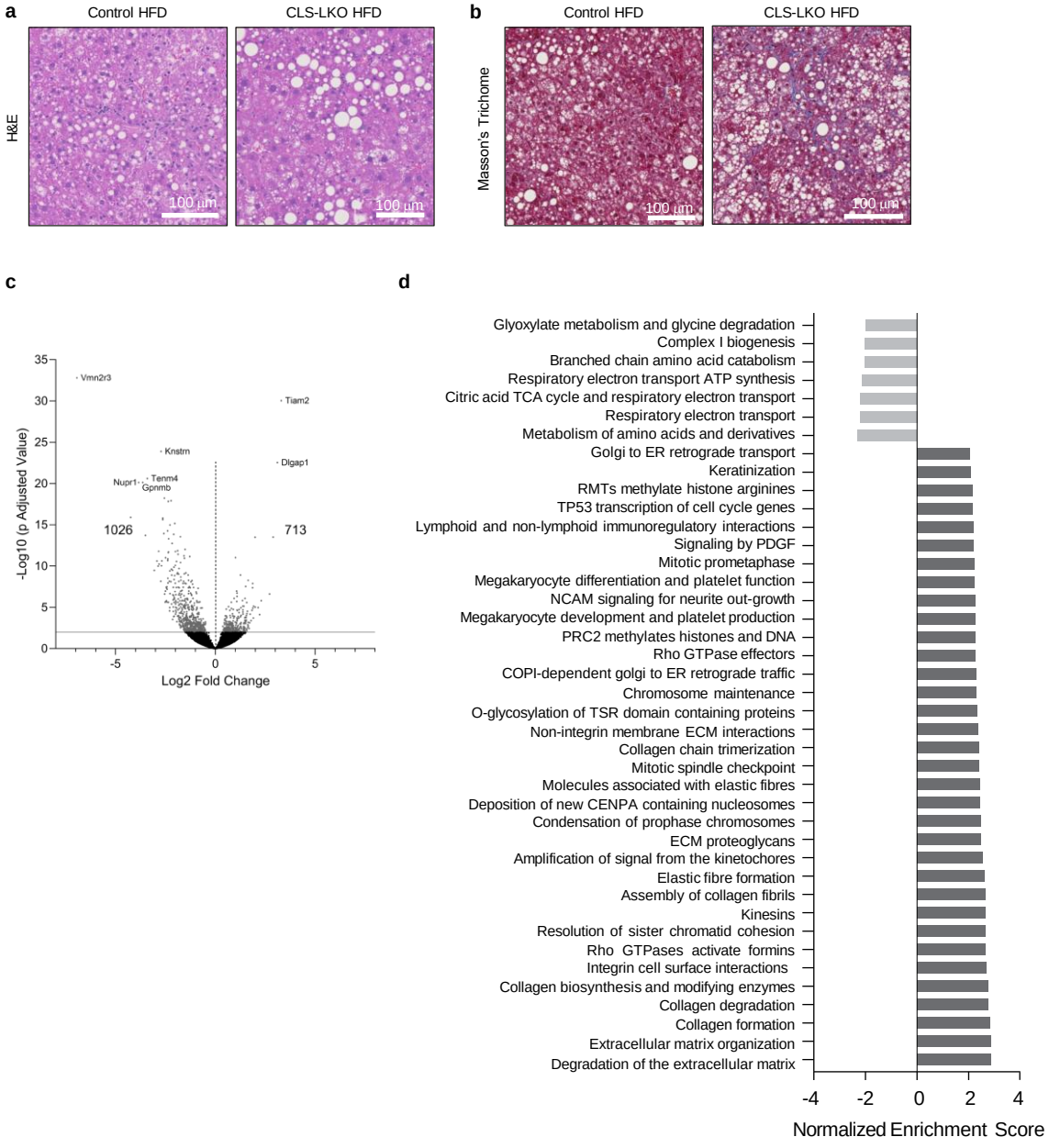

Extended Data Figure 5.

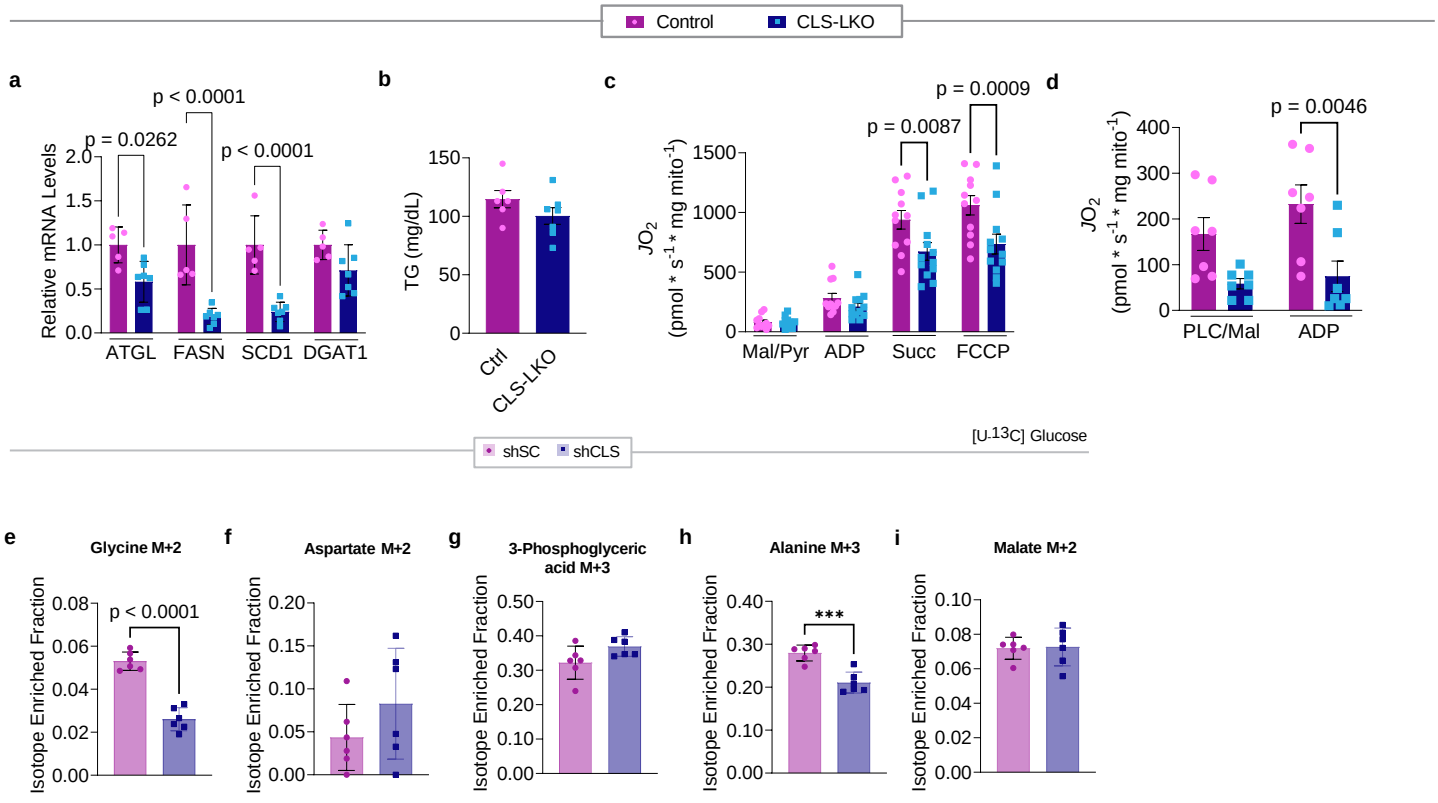

Extended Data Figure 6.

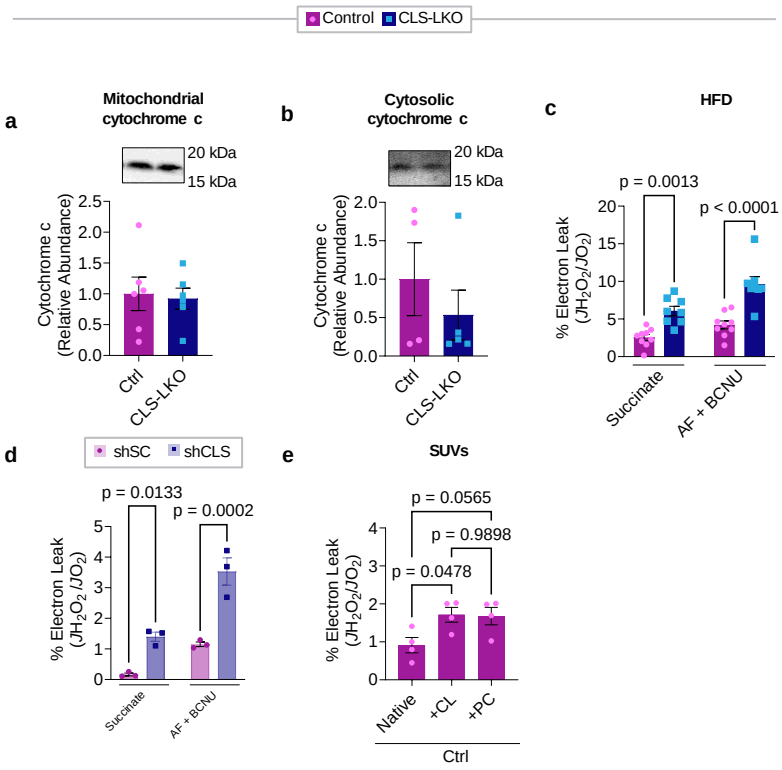

Extended Data Figure 7.

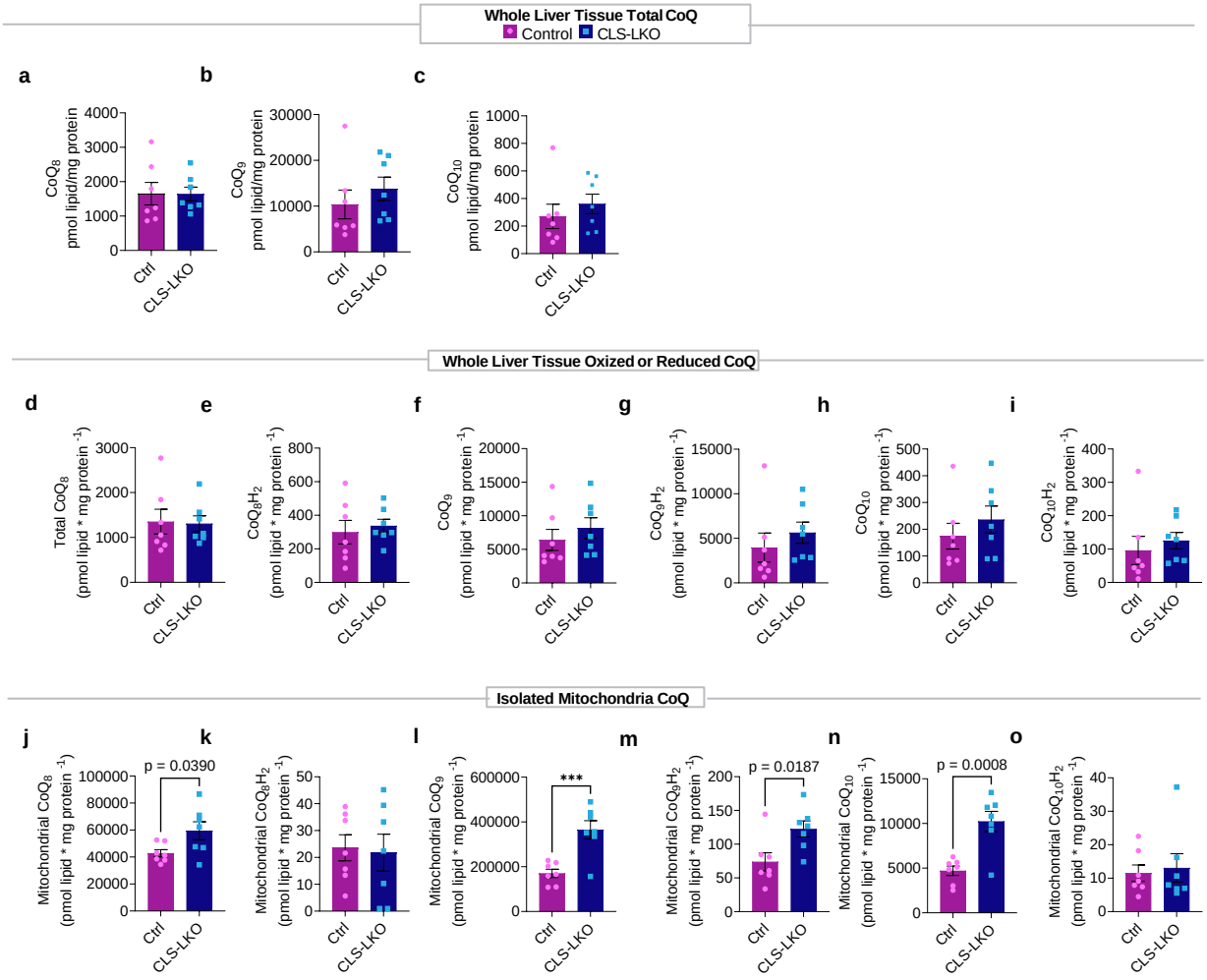

Extended Data Table 1.

Patient demographic information

	Healthy	MASH
Age at time of collection	50.3 ± 9.6 yrs	62.2 ± 7.1 yrs
Sex	Male: 1 Female: 10	Male: 9 Female: 8
Alcohol use?	N/A	Yes: 0 No: 17
Race	White: 9 African American: 1 Asian: 1	White: 10 Unknown: 7

Extended Data Table 2.

Reagents and resources

REAGENT or RESOURCE	SOURCE	IDENTIFIER
Antibodies		
GRIM19	Abcam	ab110240
SDHA	Abcam	ab14715
UQCRFS1	Abcam	ab14746
MTCO1	Abcam	ab14705
ATP5a	Abcam	Ab14748
NDUFA9	Abcam	Ab14713
Total OxPhos Antibody cocktail	Abcam	MS604-300
Citrate Synthetase	Abcam	Ab96600
Cytochrome c	Cell Signaling	11940S
Caspase-3	Cell Signaling	9661S
Caspase-7	Cell Signaling	9491S
CD16/32 (Fc Block, clone 93)	Biolegend	101308
CD45 (FITC, clone S18009F)	Biolegend	157214
CD11b (BVC421, clone M1/70)	Biolegend	101202
F4/80 (APC, clone BM8)	Biolegend	123102
TIM4 (PerCP/Cy5.5, clone RMT4-54)	Biolegend	130020
Ly6C (PE, clone HK1.4)	Biolegend	128008
MHCII (BV605, clone M5/114.15.2)	Biolegend	107639
CD11c (BV785, clone N418)	Biolegend	117302
Ly6G (PE/Cy7, clone 1A8)	Biolegend	164504
OxPhos Blue Native WB Antibody Cocktail	ThermoFisher	45-7999
Bacterial and virus strains		
Second-generation lentiviral-mediated knockdown system		
NEB Stable Competent E. Coli	NEB	C3040H
Biological samples		
Chemicals, peptides, and recombinant proteins		
Amplex Red Reagent	ThermoFisher Scientific	A12222
Auranofin	Sigma Aldrich	A6733
Carmustine (BCNU)	Sigma Aldrich	C0400
SPLASH Mix	Avanti Polar Lipids	330707
Cardiolipin Mix I	Avanti Polar Lipids	LM6003
Bovine Serum Albumin	Sigma Aldrich	A7030

Protease Inhibitor Cocktail	Thermo Scientific	78446
Tamoxifen	Sigma Aldrich	T5648
Sunflower Oil	Sigma Aldrich	S5007
TRIzol	Thermo Scientific	15596018
Mini-PROTEAN TGX Gels	BioRad	4561086
ECL	PerkinElmer	104001EA
Malate	Sigma Aldrich	M7397
Pyruvate	Sigma Aldrich	P2256
GDP	Sigma Aldrich	G7127
CL 316,243 hydrate	Sigma Aldrich	C5976
ADP	Sigma Aldrich	A5285
ATP	Sigma Aldrich	A9187
Glutamate	Sigma Aldrich	G5889
Succinate	Sigma Aldrich	S3674
Carnitine	Sigma Aldrich	8.40092
Palmitoyl-CoA	Sigma Aldrich	P9716
Palmitoyl-L-carnitine	Sigma Aldrich	P1645
SYBR Green	Thermo Scientific	A25776
4% Paraformaldehyde	Thermo	J19943-K2
Opti-MEM	Gibco	31985
DMEM	Gibco	1195-092
FBS	Gibco	10082-147
Penicillin-streptomycin	Gibco	15140122
CL for SUVs	Avanti Polar Lipids	840012
PC for SUVs	Avanti Polar Lipids	850375C
PAGE 3-12% Bis-Tris Gels	Thermo Scientific	BN1001BOX
NativePage 20x Cathode Buffer	Invitrogen	BN2002
NativePage 5% G-250 Sample additive	Invitrogen	BN2004
Nativepage 4x Sample Buffer	Invitrogen	BN2003
CoQ Standard	Cambridge Isotope Labs	CIL DLM-10279
Palmitic acid (U-$^{13}C_{16}$)	Cambridge Isotope Labs	CLM-409-0.1
D-Glucose ((U-$^{13}C_6$)	Cambridge Isotope Labs	CLM-1396-5
Critical commercial assays		
Pierce BCA Protein Assay Kit	Thermo Scientific	23227
iScript cDNA Synthesis Kit	BioRad	1708891
SDH Detection Assay Kit	Abcam	ab228560
Direct-zol RNA Miniprep Plus Kit	Zymo	R2070
DNeasy Blood and Tissue Kit	Qiagen	69504

Deposited data		
Experimental models: Cell lines		
HEK293T cells	ATCC	CTRL-3216
Hepa 1-6 murine hepatoma cells	ATCC	CRL-1830
Experimental models: Organisms/strains		
Mouse: CLS conditional knockout (CLS-cKO)	Sustarsic et al. 2018	N/A
Mouse: CLS-LKO	This paper	N/A
Mouse: Alb-Cre	Jackson Laboratory	003574
Oligonucleotides		
RT qPCR Primer ATGL F (CCACTCACATCTACGGAGCC)	www.IDTDNA.com	
RT qPCR Primer ATGL R (TAATGTTGGCACCTGCTTCA)	www.IDTDNA.com	
RT qPCR Primer DGAT1 F (GACGGCTACTGGGATCTGA)	www.IDTDNA.com	
RT qPCR Primer DGAT1 R (TCACAACACACCAATTCAGG)	www.IDTDNA.com	
RT qPCR Primer FAS F (GGATAGCTGTGTAGTGTAACCAT)	www.IDTDNA.com	
RT qPCR Primer FAS R (GGTCATCGTGATAACCACACA)	www.IDTDNA.com	
RT qPCR Primer SCD1 F (GCTCTACACCTGCCTCTTCG)	www.IDTDNA.com	
RT qPCR Primer SCD1 R (CAGCCGAGCCTTGTAAGTTC)	www.IDTDNA.com	
RT qPCR Primer CLS F (TGACCTATGCAGATCTTATTCCA)	Johnson et al. 2019	
RT qPCR Primer CLS R (TGGCAGAGTTCGGTATCTGA)	Johnson et al. 2019	
RT qPCR Primer TNFa F (CCACCACGCTCTTCTGTCTAC)	www.IDTDNA.com	
RT qPCR Primer TNFa R (AGGGTCTGGGCCATAGAACT)	www.IDTDNA.com	
RT qPCR Primer Taz F (CCCTCCATGTGAAGTGGCCATTCC)	Johnson et al. 2019	
RT qPCR Primer Taz R (TGGTGGTTGGAGACGGTGATAAGG)	Johnson et al. 2019	
mtDNA F: (TTAAGACACCTTGCCTAGCCACAC)	Mouse Primer Depot NCI/NIH	
mtDNA R: (CGGTGGCTGGCACGAAATT)	Mouse Primer Depot NCI/NIH	

nucDNA F: (ATGACGATATCGCTGCGCTG)	Mouse Primer Depot NCI/NIH	
nucDNA R: (TCACTTACCTGGTGCCTAGGGC)	Mouse Primer Depot NCI/NIH	
Recombinant DNA		
Sc	Addgene	1864
Crls1	Sigma Aldrich	TRCN0000123937
psPAX2	Addgene	12260
pMD2.G	Addgene	12259
Software and algorithms		
GraphPad Prism 9.0	GraphPad	N/A
Other		